Prediction of Cohesive Zone Length and Accurate Numerical Simulation of Delamination under Mixed-mode Loading

Chetan H. C.[1] · Subhaschandra Kattimani[1] · S. M. Murigendrappa[1]

Abstract

This article presents an approach to accurately predict the Length of Cohesive Zone (LCZ) and model delamination under mixed-mode loading. A novel expression for estimating the cohesive zone length for the structure subjected to mixed mode delamination is proposed. The proposed expression of LCZ is validated for various structural configurations like mixed-mode delamination specimen, ply-drop, and L-bend. Besides, the effect of maximum interfacial strength and element size is also investigated. A modified embedded cohesive zone model based on cohesive surface modeling is suggested to predict intralaminar and interlaminar failures in ply-drop and L-bend structures. The cohesive surfaces are inserted in 90º plies to account for the matrix cracking and along the adjacent 0º plies to model interlaminar delamination. The delamination accompanied by matrix cracking, resulting in crack kinking and migration, is predicted. The predicted numerical results are in very good agreement with the experimental results available in the literature. A fine discretization of the mesh is necessary along the cohesive zone length for the precise estimation of various energy dissipation mechanisms. Thus, the present methodology aids in the mesh design by calculating LCZ and accurately predicting the structure's failure response under mixed-mode delamination.

Nomenclature

δ	Crack opening displacement
K	Penalty Stiffness
t	Traction
G_c	Critical energy release rate
G	Shear modulus
D	Damage variable
σ_{max}	Maximum interfacial stress/strength
l_{ch}	Characteristic length of cohesive zone

✉ Subhaschandra Kattimani
subhaskatti@nitk.edu.in

[1] Department of Mechanical Engineering, National Institute of Technology Karnataka, Surathkal Srinivasnagar PO, 575025 Mangalore, India

E	Elastic modulus
M	Dimensionless parameter of length of cohesive zone
l_{ch}	Actual/numerical length of cohesive zone
β	Mode ratio parameter
η	B-K mixed-mode integration parameter
α	Power law parameter
h	Specimen/structure thickness
h^l, h_0, n, m	Fit parameters based on the type of law, loading, and material property
N_e	Number of elements
l_e	Length of each element
a	Crack length

Subscripts

I	Parameter under mode-I loading
II	Parameter under mode-II loading
Mixed	Parameter under mixed-mode loading
cr	Critical
eff	Effective
f	Final

Superscripts

∘	Finite/slender structures
∞	Infinite structures
n, t and s	Normal and two shear direction
1, 2 and 3	Principal material axes

Acronyms

CZM	Cohesive Zone Model
LCZ	Length of Cohesive Zone
FE	Finite Element
MMB	Mixed Mode Bending
MECM	Modified Embedded Cohesive Zone Model
VCCT	Virtual Crack Closure Technique
LEFM	Linear Elastic–Plastic Fracture Mechanics

1 Introduction

Polymer composite materials, especially fiber-reinforced composites, offer a distinctive material capability for low weight structures which demand high strength and stiffness. The composites can be tailored or customized to adequately match the high structural design standards of various industries like defence, aerospace, automotive, and wind energy. The failures of composite structures in numerous applications are complex phenomena with intralaminar matrix failures and interlaminar delamination failures [1, 2]. Cohesive Zone Model (CZM) is most widely used to predict delamination initiation and propagation behavior in composites. Since its inception by Dugdale [3] and Barenblatt [4], various cohesive zone models have been proposed. However, the bilinear CZM is

most simple to implement and is widely used for delamination analysis as the global load–displacement of composite structures is insensitive to the shape of the traction separation curve [5].

The cohesive zone requires an accurate representation of the stress field distribution of crack tip along the process zone. Subsequently, it requires fine discretization of the cohesive zone ahead of the crack tip to account for energy dissipation. The Length of the Cohesive Zone (LCZ) is defined as the crack plane distance wherein the cohesive forces are acting. The CZM considers the internal length, also known as the characteristic length (l_{ch}), which is a function of elastic modulus, critical fracture toughness, and interfacial stress of the material. The LCZ may vary with specimen geometry and is different for a finite/slender structure or infinite/thick structure [6]. It is very desirable and efficient to know the LCZ beforehand, thus making the investigations a good compromise between accuracy and computational cost. Analytical expressions proposed in most of the literature have limiting conditions such as infinite structure and finite structure or a generalized expression for LCZ under pure and mixed modes of loading [7, 8]. However, expressions to predict LCZ for delamination under mixed-mode loading for composite structures of any thickness are not found in the literature. The current work focuses on the prediction of LCZ based on the analytical bounds for finite and infinite expression for mixed-mode loading.

As the failures of composites are known for their complexity, accurate estimation of structural response would require progressive damage simulation with high fidelity. As standard simulation techniques are not suitable to predict such failures, many numerical models based on CZM and other FE models have been proposed [9–14]. Even though the use of methods other than CZM is more accurate, the computational effort and cost required to numerically model large structures or complex shapes are immense. The use of cohesive behavior has shown encouraging results in many previous studies. Also, unlike most numerical models, substantial relation cannot be established between in-plane matrix damage and delamination [15].

On similar grounds, many models have been proposed for simple composite specimen configurations [16–25]. However, numerous interfacial element behavior in all the layers of a large composite structure would be computationally inefficient. To predict intralaminar and interlaminar failure of complex shapes like L bend, Cao et al. [26] inserted interfacial behavior in 90º lamina as potential matrix cracking was bound to happen. Further, in composite materials, the effect of LCZ in discretization is overlooked in the literature. To attain a numerically accurate and computationally efficient model, it is necessary to consider the various length scale or LCZ for the discretization of the model. The current study tries to improve the capabilities of the embedded cohesive zone technique by considering the length scale or LCZ under mixed-mode loading. Henceforth, the work focuses on the accurate capture of stress variation ahead of the crack tip and the precise prediction of load–displacement behavior of the structure.

The present study aims to propose an analytical equation for the prediction of LCZ for mixed-mode delamination for any specimen configuration by a detailed investigation of existing analytical equations. The work also aims to predict the load–displacement behavior accurately by modeling intralaminar and interlaminar behavior, such as crack migration under mixed-mode loading. Further, the expression for LCZ for mixed-mode delamination is also formulated. The proposed expression is validated for standard fracture toughness specimens as well as other structural components such as ply-drop and L bend. Finally, a modified embedded cohesive zone model is proposed based on the LCZ estimation for an accurate prediction of structural behavior.

2 Background

2.1 Cohesive Zone Model and Cohesive Surfaces

The cohesive surface [27, 28] has zero thickness, or interface thickness is negligibly small. The traction separation law considers initial linear elastic behavior, succeeded by initiation and damage evolution. The relative displacement along the interface surface is denoted as 'δ', and the traction separation behavior of the cohesive zone can be represented as shown in Fig. 1.
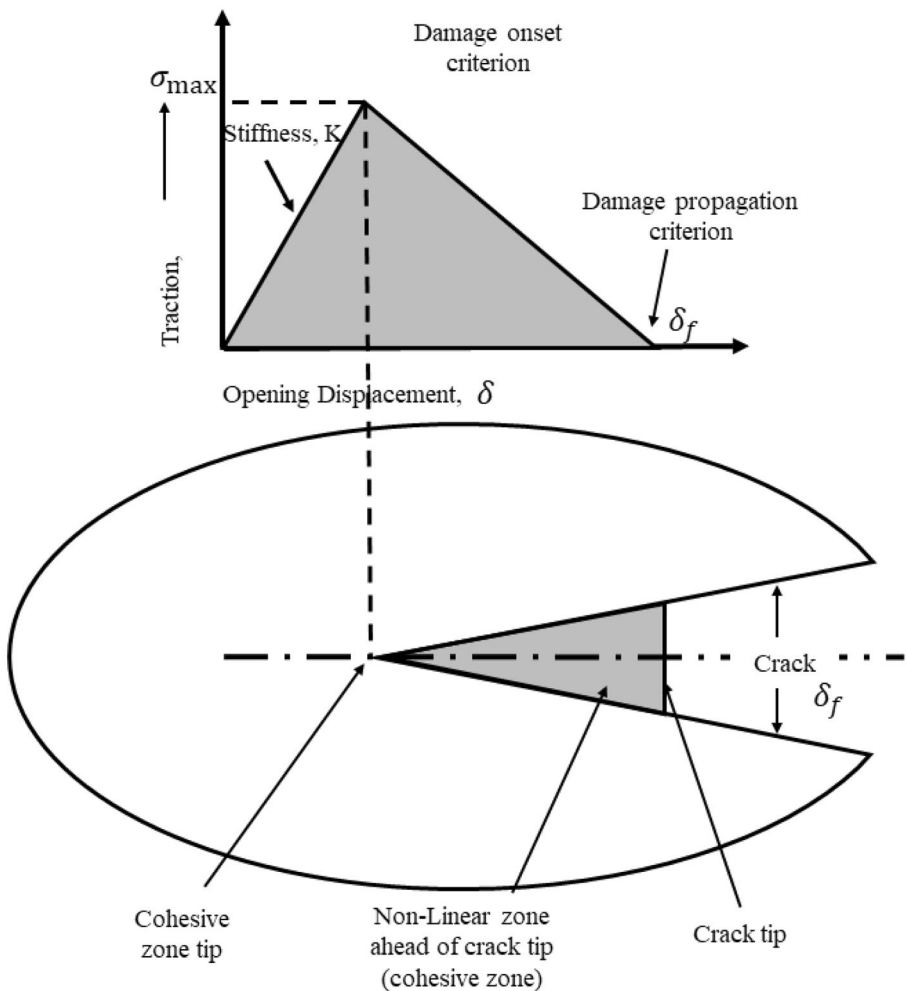
The elastic behavior can be represented as

Fig. 1 Traction separation response of cohesive zone model

$$t = \begin{Bmatrix} t_n \\ t_s \\ t_t \end{Bmatrix} = \begin{bmatrix} K_{nm} & K_{ns} & K_{nt} \\ K_{ns} & K_{ss} & K_{st} \\ K_{nt} & K_{st} & K_{tt} \end{bmatrix} \begin{Bmatrix} \delta_n \\ \delta_s \\ \delta_t \end{Bmatrix} = K\delta \tag{1}$$

where 't' denotes the traction vector, 'K' represents the stiffness. The subscripts n, t, and s depict the normal (mode-I), tangential (mode-II), and shear tractions (mode-III), respectively.

The tractions acting at the interface can be represented as

$$t_{(n,s,t)} = (1 - D)\bar{t}_{(n,s,t)} \tag{2}$$

The variable 'D', represents the irreversible damage, with $D = 0$ and $D = 1$ depicting no damage and completely damage states, respectively.

To represent the damage under the combined mode of loading with both normal and shear components acting across the interface, an expression for effective separation is defined as

$$\delta_m = \sqrt{\langle \delta_n \rangle^2 + \delta_s^2 + \delta_t^2} \tag{3}$$

The damage evolution is dependent on the energy released during the surface separation process. The energy dissipated during the process is called fracture energy and is equal to the area under the traction separation curve. The dependence of fracture energy (G) on mixed-mode can be represented either by power-law as

$$\left\{ \frac{G_n}{G_n^C} \right\}^\alpha + \left\{ \frac{G_s}{G_s^C} \right\}^\alpha + \left\{ \frac{G_t}{G_t^C} \right\}^\alpha = 1 \tag{4}$$

or by B-K criteria [29] as

$$G_{mc} = G_{IC} + \left(G_{IIC} - G_{IC} \right) \left(\frac{G_{II}}{G_I + G_{II}} \right)^\eta \tag{5}$$

The parameter 'α' and 'η' represent power law and B-K law coefficient, respectively.

The failure process is governed by damage factor is estimated based on the deformation and accumulated damage history as

$$D = \frac{\delta_m^f \left(\delta_m^{max} - \delta_m^0 \right)}{\delta_m^f \left(\delta_m^f - \delta_m^0 \right)} \tag{6}$$

where,

$$\delta_m^f = \frac{2G^c}{T_{eff}^0} \tag{7}$$

T_{eff}^0 is effective traction and δ_m^{max} is maximum effective separation at damage initiation.

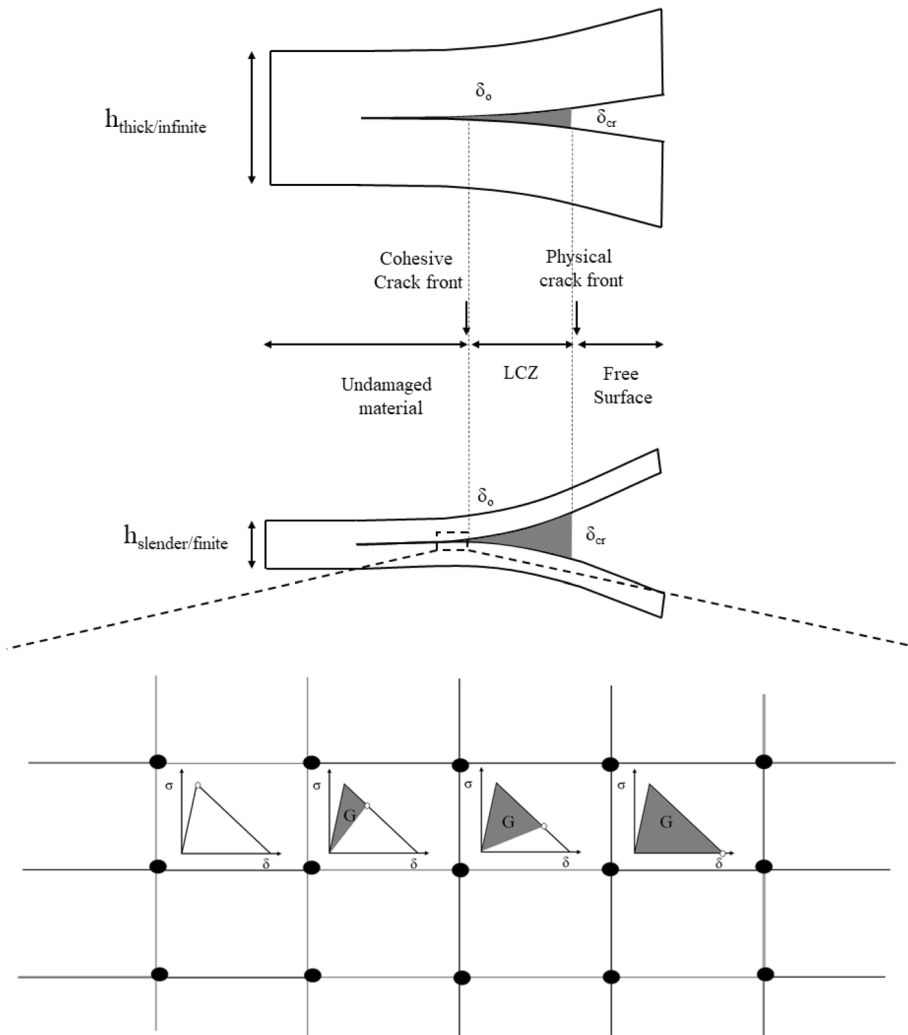## 2.2 Length of Cohesive Zone

Many authors have proposed various analytical expressions to estimate the LCZ. For the case of ductile solids, Irwin [30] proposed that the cohesive zone length is considered the size of the plastic zone ahead of a crack when Von Mises stress exceeds the tensile yield stress at the crack tip. Dugdale [3] measured the length of the plastic zone for a thin elastic sheet with center crack by assuming yielding to be a very narrow strip along the line ahead of the crack tip. Barenblatt [4] proposed a cognate of Dugdale's plastic zone analysis for ideally brittle materials. The length of the cohesive zone for soft elastic solids was estimated based on linear viscoelastic fracture mechanics by Hui [31]. Falk et al. [32] predicted a cohesive length scale as a function of crack propagation and branching velocities. The cohesive zone length scale was determined by elastic properties, strength, and surface energy. Hillerborg et al. [33] proposed the use of characteristic length parameters in concrete. They assumed that the crack would propagate when the stress at crack trip reaches the material's tensile strength, and there is a gradual decrease in the stress with an increase in the crack opening. Assuming the stress intensity factor at the crack tip and crack opening should be equal to that of the critical value, Cox and Marshall [34] proposed the length of cohesive zone based on the bridged crack theory. Similarly, Bazant [35] established cohesive zone length for concrete. It can be noted that all the expressions proposed are of the form

$$l_{ch} = \frac{EG_c}{\sigma_{I,max}} \tag{8}$$

$$l_{cz} = M \times l_{ch} \tag{9}$$

where E, G, M are dependent on the cohesive zone model. Bazant et al. [35, 36] also investigated the size effect on fracture energy and characteristic cohesive process zone length. Both fracture energy and process zone length were expressed as a function of specimen thickness. Therefore, it is convenient to predict the characteristic length in simple fracture toughness specimens compared to geometrically similar structures or specimens of different sizes and thicknesses. It is also assumed that the nominal stress depends on the specimen geometry. In contrast, the relative displacement of a simple, slender structure is more than that of a thick structure, as shown in Fig. 2. It is an effect of slender specimens having shorter LCZ as compared to thick specimens along the crack propagation plane.

The studies done by Yang et al. [37] used CZM to analyze the nonlinear process of material failure. The representation of nonlinear deformation attributes to micro failures occurring in the fracture process zone. Analogously, various forms or shapes of cohesive zone models are used based on the fracture process at the micro-scale, thus varying the fracture process zone along with the crack propagation. Consequently, cohesive zone length depends on the thickness of the specimen or structure, cohesive shape, and characteristic length.

Stress Distribution

Fig. 2 Effect of size of structure and stress distribution along the cohesive zone

2.3 Length of a Cohesive Zone for Infinite Structures

The analytical solutions of cohesive zone length for infinite structures do not influence the material depth or thickness as the fracture process zone is much smaller than the specimen size. Turon et al. [38] defined the length of the cohesive zone for infinite structure as:

For mode-I and mode-II

$$l_{cz,I}^{\infty} = M_I \frac{E_I' G_{Ic}}{\left(\sigma_{I,max}\right)^2} \tag{10}$$

$$l_{cz,II}^{\infty} = M_{II} \frac{E_{II}' G_{Ic}}{\left(\sigma_{II,max}\right)^2} \tag{11}$$

For mixed-mode

$$l_{cz,mixed}^{\infty} = M_{mixed} \frac{E_m G_{Ic}}{\left(\sigma_{mixed,max}\right)^2} \tag{12}$$

where,

$$E_m = E_I^1(1 - \beta) + E_{II}^1 \beta \tag{13}$$

$$\beta = \frac{G_{II}}{G_I + G_{II}} \tag{14}$$

$$G_c = G_{Ic} + \left(G_{IIc} - G_{Ic}\right)\beta^{\eta} \tag{15}$$

$$\sigma_{mixed} = \sigma_{I,max}^2 + \left[\sigma_{II,max}^2 - \sigma_{I,max}^2\right]\beta^{\eta} \tag{16}$$

where M is a dimensionless factor defined based on the model or constitutive relation and mode of fracture. For the various form of the softening law, Smith [39] predicted the length of the fracture process zone for structures subjected to pure mode I loading. The value of M was deduced to be $\pi/8$ for an infinite solid and 0.760 for a double cantilever beam. To analyze the evolution of the fracture process zone for infinite specimens, Planas and Elice [40, 41] presented an asymptotic analysis method. The analysis was utilized to investigate the effect of size and shape of cohesive law on the length of the cohesive zone. The authors established the values of M equal to $\pi/8$ for constant, 0.731 for linear, and 2.92 for quasi exponential softening models. Hence, justifying the variation of length of the zone is influenced by the shape of cohesive law and the thickness of the structure. Bao and Suo [42] emphasized the concept of large-scale bridging to estimate the length of the process zone.

Similarly, Suo and Bao [43] established the variation of process zone with the increase in the specimen thickness for mode-I, mode-II, and mixed-mode loading. Harper and Harlett [44] investigated the effect of strength, fracture toughness, and youngs modulus on cohesive zone length.

2.4 Length of a Cohesive Zone for Slender Structures

The analytical expressions discussed in the previous section are for infinite bodies where the structure's thickness does not affect the length of the cohesive zone. However, it is demanding to analyze the effect of thickness for many practical engineering applications due to the slender character in most of the composite laminates. In most failures like

delamination and bond line failure, the thickness of the specimen might be less or comparable with the length of the cohesive zone. To investigate the thickness effect on the length of the cohesive zone for a range of cohesive laws, William et al. [45] proposed an analytical solution of equivalent crack length for elastic materials. Smith [39] proposed a theory for the slender body under pure mode -I loading and obtained dimensionless parameter M = 1/3 for constant and 1 for linear softening law.

In a relatively slender body, the expression to predict characteristic length under mode-I loading is as follows:

$$l_{cz_{I,slender}} = M_{I,Slender} \left(\frac{E^1_{I^{slender}} G_c}{\sigma_{I,max}} \right)^{1/4} \times h^{3/4} \tag{17}$$

where h is half the thickness of the laminate, and M = 1/3 is a non-dimensional scale parameter for constant cohesive law. The equivalent elastic modulus, E^1 is a function of E_{11}, E_{22} and G_{12}, which are presented in Appendix 1.

Massabo and Cox [46] investigated delamination cracks subjected to mode II loading for through-thickness bridging. An analytical expression for the length of the cohesive zone for mode II can be written as

$$l_{cz_{II,slender}} = M_{II,Slender} \sqrt{ \left(\frac{E^1_{II^{slender}} G_c}{\sigma_{II,max}} \right) \times h } \tag{18}$$

Turon et al. [47] proposed a methodology to predict the LCZ under mode I, mode II and mixed-mode loading based on the relation of characteristic length and size effect on the structure. Authors also assumed that in finite-size structures, the unstable crack propagates at an energy level less than the actual fracture toughness of the material, and the length of the process zone is comparably small. The analytical solution for the length of cohesive prediction is expressed as.

For mode-I

$$l_{cz_{I,slender}} = \frac{h}{(h + h_I)} l^\infty_{cz,I} \tag{19}$$

For mode-II

$$l_{cz_{II,slender}} = \frac{h}{(h + h_{II})} l^\infty_{cz,II} \tag{20}$$

For mixed-mode

$$l_{cz_{mixed,slender}} = \frac{h}{(h + h_0)} l^\infty_{cz,mixed} \tag{21}$$

where h is the length, which is a function of material and structure. The dimensionless scale parameters, M and h_0 depend on the type of loading and shape of cohesive law.

2.5 Generalised LCZ Expressions

It can be noted that in the various comprehensive applications, LCZ cannot be estimated accurately. To the best of the authors' knowledge, very few studies attribute to the estimation of LCZ for any thickness, structure, and type of loading. Harper and Hallett [48] proposed a scaling factor of 0.5 to be multiplied with a minimum LCZ value obtained among analytical expressions from both finite and infinite length. The length was estimated for a bilinear traction separation law under mixed-mode loading. However, the solution does not remain valid for variation in crack length, mode ratio, and structure geometries.

$$l_{cz,predicted} = 0.5 \left[min(Eq.\ 10,\ Eq.\ 11,\ Eq.\ 17,\ Eq.\ 18) \right] \tag{22}$$

Soto et al. [7] presented an empirical expression to estimate the LCZ for orthotropic material under mode I and Mode II loading as

$$l_{cz,I} = \left(l_{cz,I}^{0\ -n_I} + l_{cz,I}^{\infty\ -n_I} \right)^{-\frac{1}{n_I}} \tag{23}$$

$$l_{cz,I} = \left(l_{cz,II}^{0\ -n_{II}} + l_{cz,II}^{\infty\ -n_{II}} \right)^{-\frac{1}{n_{II}}} \tag{24}$$

where n is a fitting parameter based on the type of cohesive law and loading, the solution provides a reasonably good agreement of cohesive zone length for any structural variations in geometry and characteristic length for pure loading modes only. However, the investigation of delamination under mixed-mode loading is integral for LCZ estimation. Thus, the consecutive section provides details of an analytical expression for the prediction of LCZ for delamination under mixed-mode loading.

3 Expression of LCZ for Mixed-mode Delamination

The solution proposed by Soto et al. [7] using the statistical investigation is limited to mode-I and mode-II loading. Numerical analysis by Turon et al. [47] and Harper et al. [48] under-predicts the length of the cohesive zone under a wide range of situations. Besides, Eqs. (22)—(24) analytical solutions are inconsistent in determining the length in various intermediate scenarios for delamination under mixed-mode loading. Subsequently, it is pertinent to deduce a solution to estimate the length of the cohesive zone for a structure of any thickness subjected to mixed-mode loading. Consequently, to predict LCZ for any structure and the transitional situation between finite to infinite, the current work proposes an asymptotic regression model for mixed-mode delamination as follows:

$$l_{cz,mixed}^{\circ\infty} = l_{cz,mixed}^{\infty} + \left(l_{cz,mixed}^{\circ} - l_{cz,mixed}^{\infty} \right) e^{-mh} \tag{25}$$

where h is the thickness of structure; m is the fitting parameter based on the type of traction separation law and material orthotropy.

By substituting Eqs. (12) and (21) in Eq. (25) for predicting LCZ in finite and infinite thickness structures, the following relation is obtained:
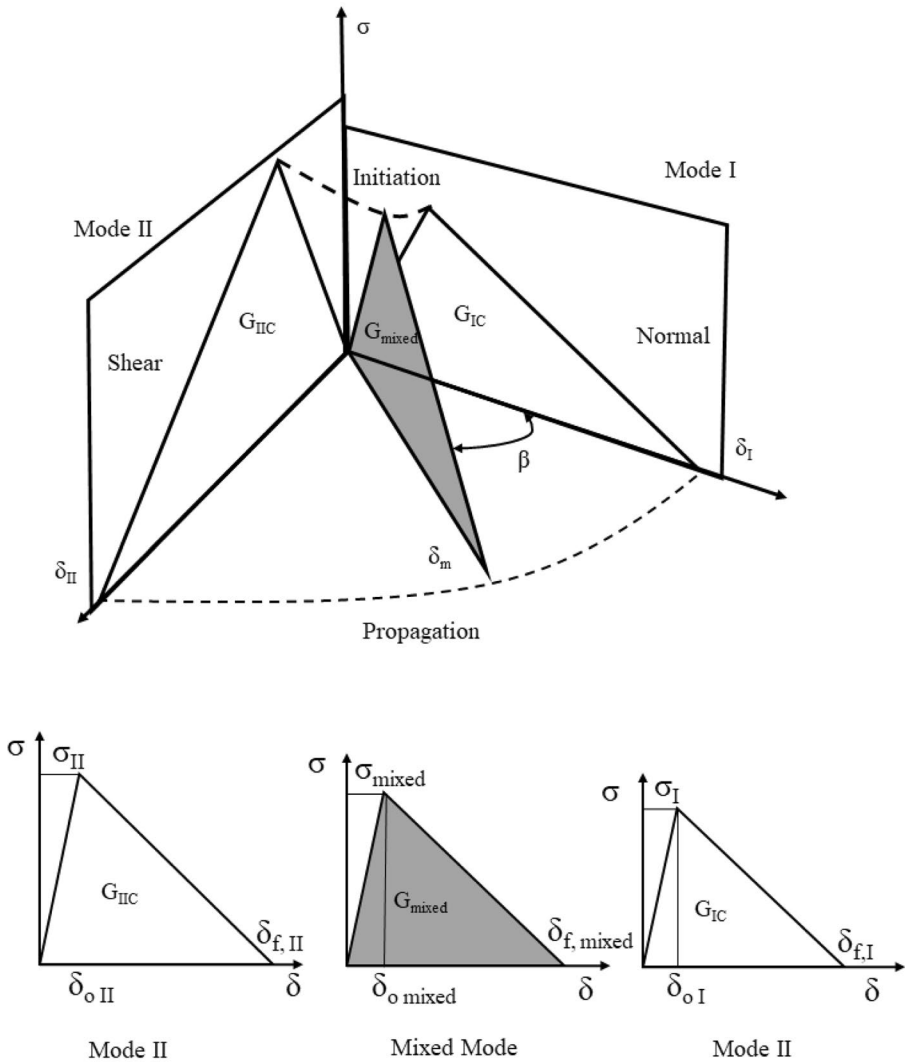
Fig. 3 Bi-linear traction separation law for mixed-mode loading

$$l^{\circ\infty}_{cz,mixed} = l_{ch,mixed}\left[M^{\infty}_{mixed} + \left[\left(\frac{h}{h+h^1}\right)M^0_{mixed} - M^{\infty}_{mixed}\right] \times e^{-mh}\right] \tag{26}$$

A numerical analysis was performed to estimate and investigate the suitability of the solution for different fitting parameters. The studies were performed using Abaqus [49] software with standard cohesive surfaces established on the contact pair algorithm and cohesive zone model approach. The current numerical study with cohesive surfaces is restricted to cohesive law with bilinear softening for mixed-mode, as in Fig. 3. Since Eq. (26) is a function of the characteristic length (l_{ch}) and specimen thickness (h), a parametric investigation was performed for various structural depths. A wide range of specimen thicknesses ($0.5 \text{ mm} < h < 40 \text{ mm}$) is considered for the analysis. A mixed-mode

Table 1 Material Properties for AS4/PEEK	Laminate Property		Interfacial Properties	
	E_{11} (GPa)	122.7	G_{Ic} (N/mm)	0.969
	$E_{22} = E_{33}$ (GPa)	10.1	G_{IIc} (N/mm)	1.719
	$G_{12} = G_{13}$ (GPa)	5.5	$\sigma_{I, max}$ (MPa)	80
	G_{23} (GPa)	3.7	$\sigma_{II, max}$ (MPa)	100
	$\nu_{12} = \nu_{13}$	0.25	K_I (N/mm^3)	10^6
	ν_{23}	0.45	K_{II} (N/mm^3)	10^6

configuration specimen [50] of 102 mm long and an initial crack of 39.3 mm is considered. The built-in plane strain, CPE4I element from Abaqus [49], was used with a minimum of 10 elements through thickness. The material properties used are given in Table 1. The B-K criteria is used to predict delamination with $\eta = 2.284$ [29].

The exponent m and other fit parameters from Eq. 26 were obtained using the least square method for the mode ratio of 50% and 80%, as shown in Figs. 4 and 5, respectively. It is observed that the parameters are dependent on the material property as well as a mixed-mode ratio. The prediction of parameters for variation in mode ratios is listed in Table 2. Figures 6 and 7 show a comparison between the proposed analytical solution and other existing analytical solutions from the literature. As discussed in
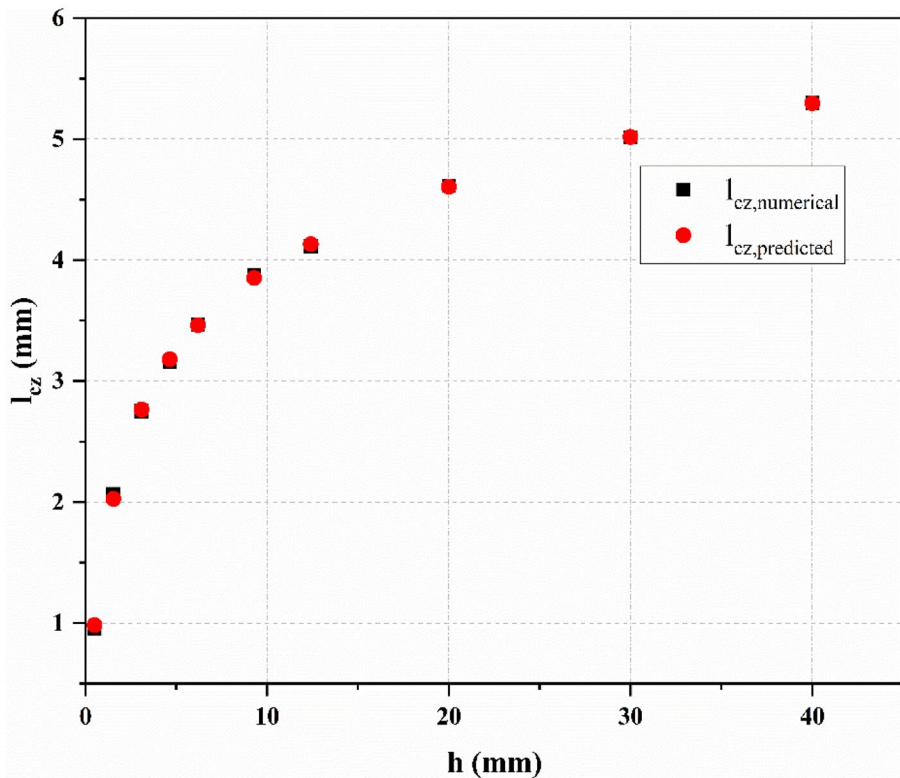
Fig. 4 Numerical and predicted l_{CZ} results for MMB with 50% mode ratio
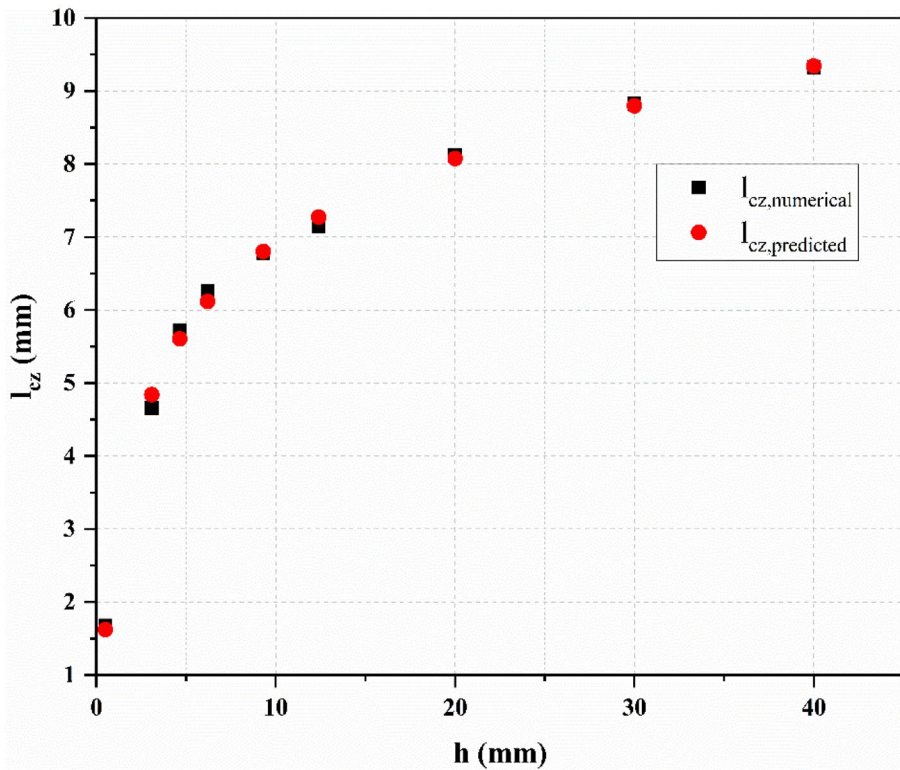
Fig. 5 Numerical and predicted l_{cz} results for MMB with 80% mode ratio

previous sections, it is evident from the result that the existing analytical solutions for mixed-mode delamination either underestimate or overestimate the LCZ. However, the present analytical solution (Eq. 26) for mixed-mode delamination prediction concurs with numerical results. It can be noted from Figs. 6 and 7 that for the low thickness values, the solution obtained by Turon [47] gives a relatively close match to the numerical results, but as thickness increases, the estimation is inaccurate. In comparison, the current analytical solution provides a better estimation.

To ascertain the relative error as the discrepancy amongst numerical solution, the proposed model, and other analytical solutions from the literature, the relative error (RE) is calculated by Eq. (27). From Figs. 8 and 9, it is observed that the relative error for LCZ estimations made from the existing literature can be as high as 370%

Table 2 Fitting parameters

| Parameters	Mode ratio	
	50%	80%
h^1	1.495677	1.786554
M^0	0.695424	0.998026
M^∞	1.155511	1.669675
m	0.032405	0.01884
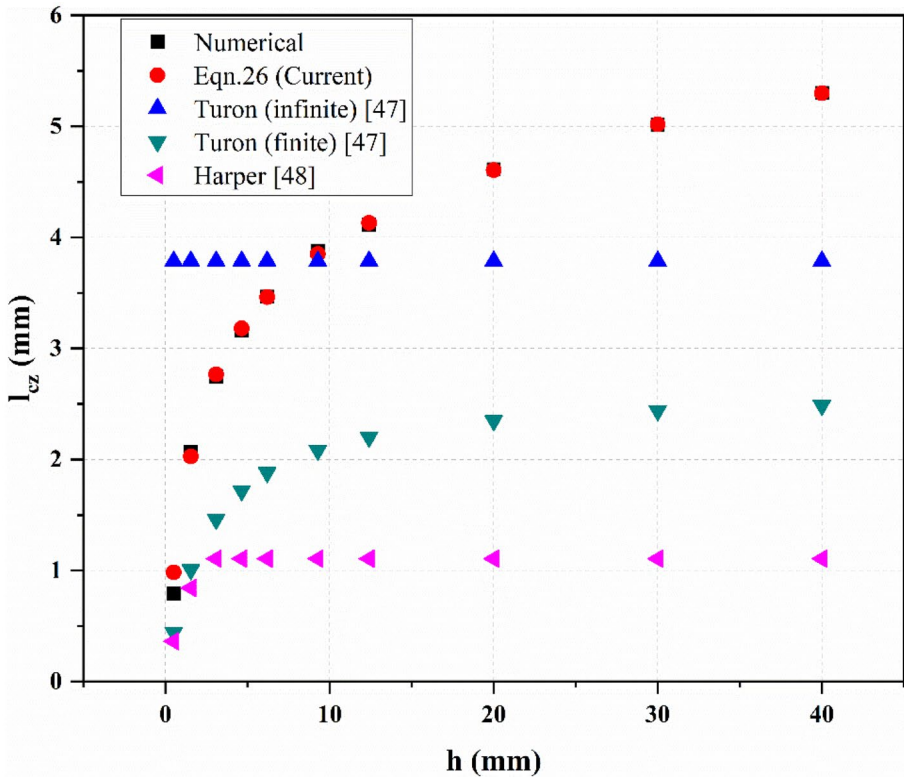
Fig. 6 Comparison of numerical results for mixed-mode Eq. 26 (current model) with the Turon's infinite and finite expression [47], Harper's expression [48] for mode ratio 50%

and 140% for 50% and 80% mode ratio, respectively. On the other hand, the relative errors by the present solutions are well below 2% and 2.9% for 50% and 80% mode ratio, respectively. Thus, except for an initial underestimation with 23% for 50% mixed-mode ratio, the predicted LCZ is in close agreement with numerical studies.

$$RE(\%) = \left| \frac{l_{cz,exact} - l_{cz,estimated}}{l_{cz,exact}} \right| \times 100 \qquad (27)$$

From the proposed analytical solution (Eq. 26), the length of the cohesive zone for a wide range of situations which fall between finite and infinite thickness bounds can also be estimated.

4 Numerical Determination of LCZ

The numerical LCZ is interpreted as the length of the interface over which elements lie in the softening region of the traction separation curve, i.e., the distance from the initial node where the interfacial strength is maximum to the node where the strength
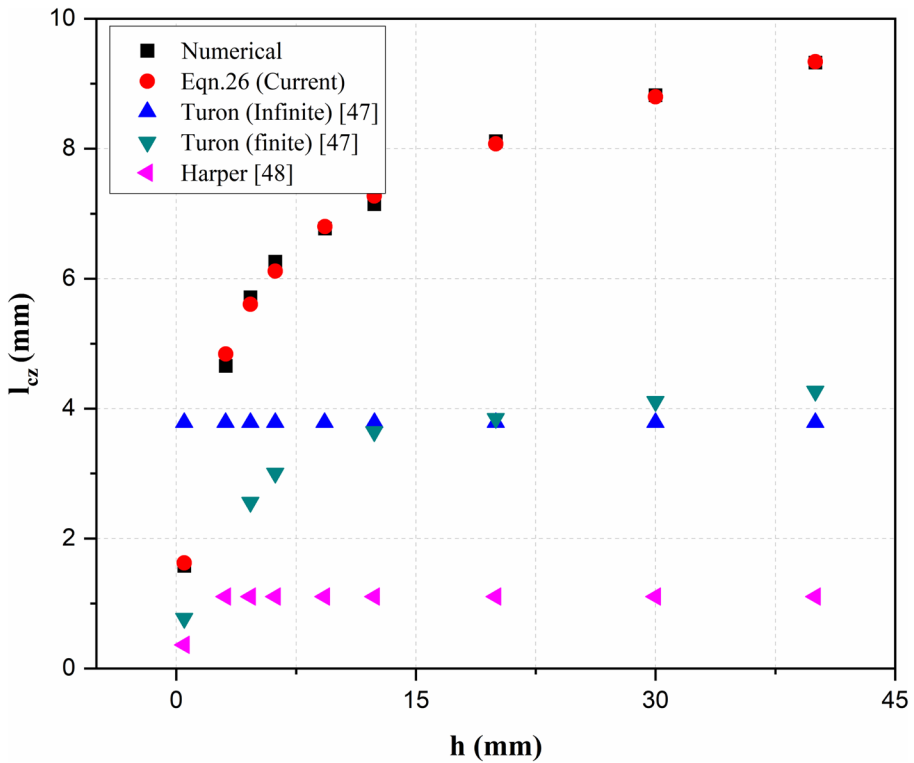
Fig. 7 Comparison of numerical results for mixed-mode with Eq. 26 (current model), Turon's infinite and finite expression [47], Harper's expression [48] for mode ratio 80%

is zero. In this section, the applicability of the proposed analytical solution is validated for standard fracture toughness specimens and for a few structural component configurations under mixed-mode loading. In addition, further investigation is carried out to validate the influence of element size and interfacial strength on structural response.

4.1 Standard Fracture Toughness Specimen: MMB

In this section, to substantiate the proposed analytical solution for the prediction of LCZ and verify the influence of mesh size and interfacial strength, standard fracture toughness specimen under mixed-mode bending delamination is analyzed. The specimen simulated is 150 mm long, with two 1.55 mm thick arms, and with an initial crack length of 35 mm, as shown in Fig. 10. The material property for numerical analysis is given in Table 3. The B-K criteria is used to predict delamination, $\eta = 2$, and the mixed-mode ratio of 50% [51].

The FE model consists of CPE4I, a plane strain element from Abaqus/ Standard. The two arms are defined with cohesive surface behavior with a minimum of ten elements through-thickness and element size of 0.15 mm along the length of the specimen.

Several simulations with the same material property with different arm thickness h were performed to predict LCZ. The fit parameters in the proposed solution were obtained by the least-square fitting method. Based on Eq. (26), the LCZ for mixed-mode bending
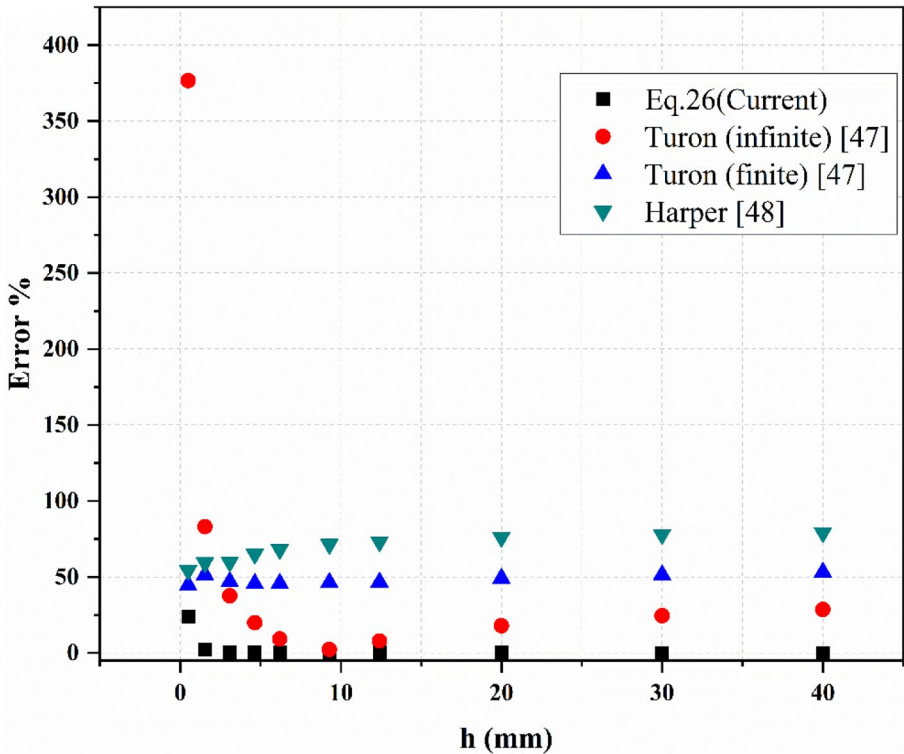
Fig. 8 Comparison of the error percentage for mixed-mode with Eq. 26 (current), Turon's infinite and finite expression [47], Harper's expression [48] for mode ratio 50%

delamination is 1.9133 mm ($h^1 = 2.4931$, $M^0 = 0.517613$, $M^\infty = 0.537133$, $m = 0.021433$). The numerically obtained LCZ is 1.9834 mm. This value is close to the predicted value from the model. Several other simulations were carried out to investigate the effect of element size ranging from 0.125 mm to 4 mm and interfacial strength ranging from (15 MPa $\leq$ Mode-I $\leq$ 40 MPa; 30 MPa $\leq$ Mode-II $\leq$ 90 MPa).

The load–displacement curves are obtained for the simulation at the loading point and are compared with the analytical solution based on the LEFM approach (Appendix 2). It can be noted that with element size greater than 1 mm, numerical results are not in convergence with analytical solutions, as shown in Fig. 11. The LCZ can also be defined as

$$l_{cz} = N_e l_e \tag{28}$$

where, N_e is the number of elements in the damage zone, and l_e is the length of each element.

Hence, as per Eqs. (26) and (28), the element size should be less than a millimeter to accommodate a minimum of three elements in the cohesive zone. The applied load and displacement relation in Fig. 12 exhibits quite good agreement with the analytical curve, except for a few cases. With the variation of interfacial strength, a variation of predicted peak load is noted. This can be attributed to the variation of the energy release rate with
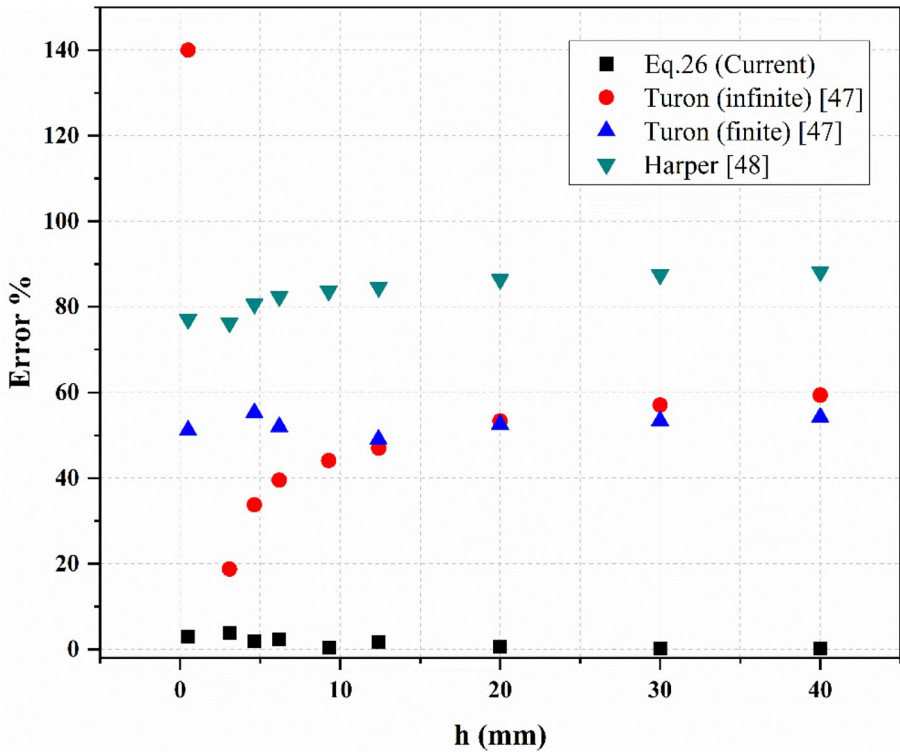
Fig. 9 Comparison of the error percentage for mixed-mode with Eq. 26 (current), Turon's infinite and finite expression [47], Harper's expression [48] for mode ratio of 80%

an increase in interfacial stress [28]. It can be ascertained with inequitable variation/reduction of interfacial strength (15 MPa, 30 MPa). As a result, the shape of the initiation curve changes, and the solution does not converge with the analytical curve. Hence, it can be
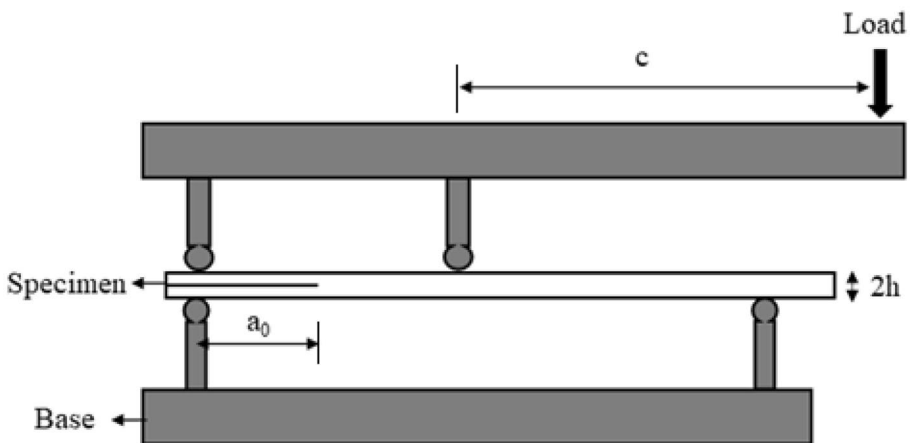

Fig. 10 Mixed Mode Bending (MMB) specimen configuration

Table 3 Material property for mixed-mode specimen

Laminate Property		Interfacial Properties	
E_{11} (GPa)	120	G_{Ic} (N/mm)G_{Ic} (N/mm)	0.260
$E_{22} = E_{33}$ (GPa)	10.5	G_{IIc} (N/mm)	1.002
$G_{12} = G_{13}$ (GPa)	5.25	$\sigma_{I, max}$ (MPa)	30
G_{23} (GPa)	3.48	$\sigma_{II, max}$ (MPa)	60
$\nu_{12} = \nu_{13}$	0.3	K_I (N/mm^3)	10^6
ν_{23}	0.5	K_{II} (N/mm^3)	10^6

confirmed that mixed-mode delaminations are a strength-sensitive failure process compared to mode-I and mode-II [52].

4.2 Structural Component: Ply-drop

In this section, a simple ply-drop specimen [44] is analyzed. Various advanced lightweight composite structures, especially defence and aerospace structures, have a complicated shape with through-thickness variations [53, 54]. The tapering can be achieved by terminating the lamina resulting in a ply-drop. As eventuate of material discontinuity in the geometry, ply-drop induces stress concentration, causing the onset of failure.
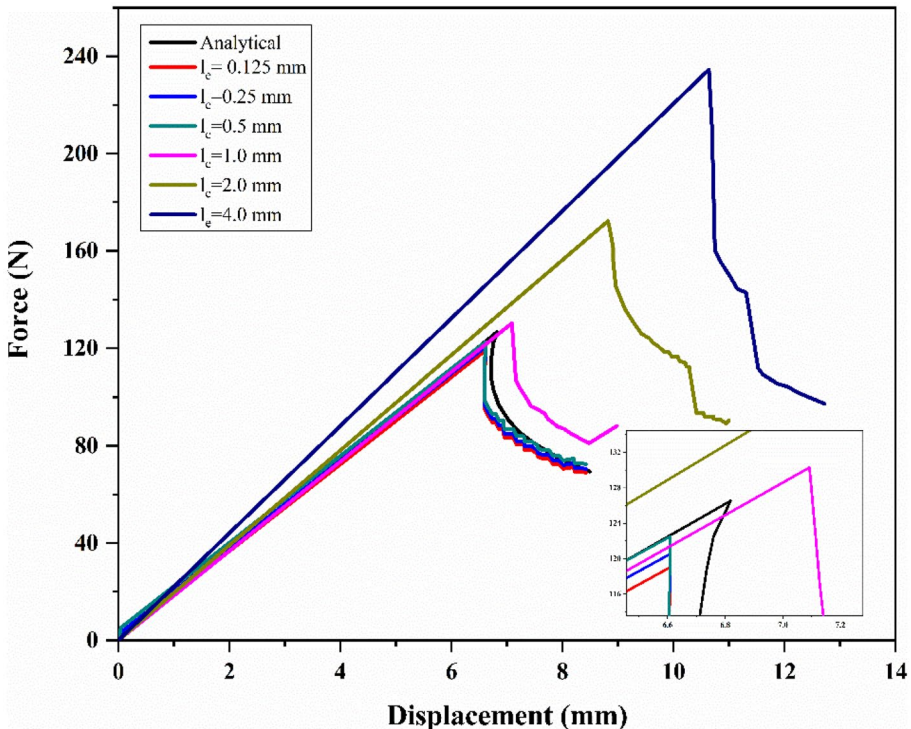
Fig. 11 Effect of element size on load vs. displacement behavior for MMB
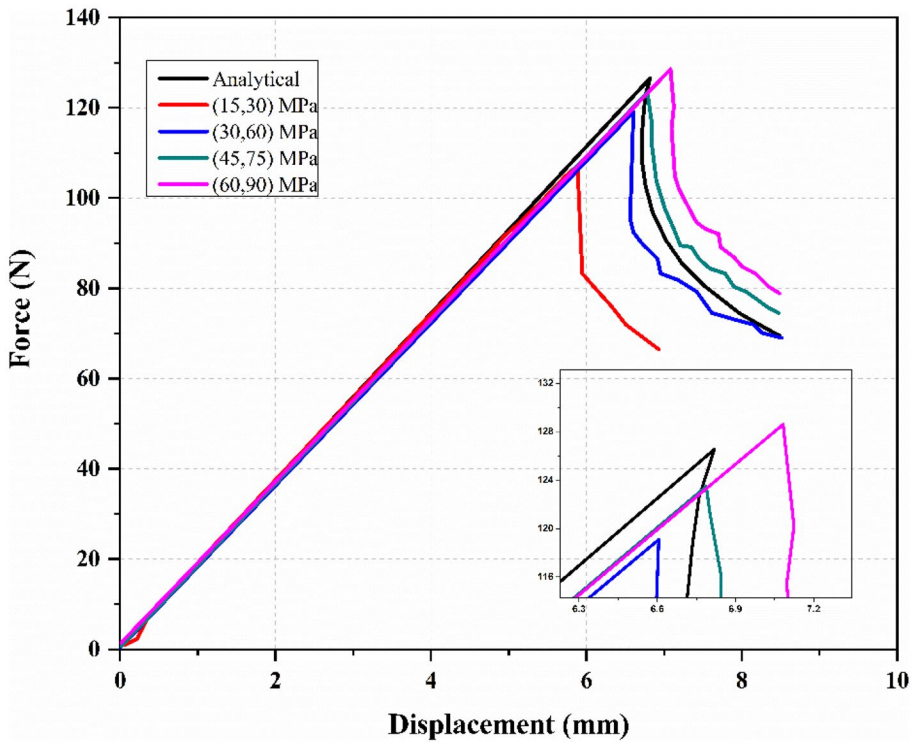
Fig. 12 Effect of interfacial stress on load vs. displacement behavior for MMB

In this study, a numerical ply-drop model without initial crack, as shown in Fig. 13, is considered for the analysis. A quarter model of symmetric external ply-drop with 16 unidirectional plies and four ply-drop on either side of the core is analyzed, as depicted in Fig. 13. The thickness of each ply is 0.65 mm, and that of the core is 2.6 mm. The plies and core are modeled with plane strain elements. A cohesive contact behavior is established between the final ply-drop and core. The material properties used for the modeling are tabulated in Table 4. To verify the nature of the failure process, the interfacial strength and element size is varied in the range of (0.125 mm to 4 mm) and (15 MPa $\leq$ Mode-I $\leq$ 60 MPa; 30 MPa $\leq$ Mode-II $\leq$ 90 MPa) respectively.
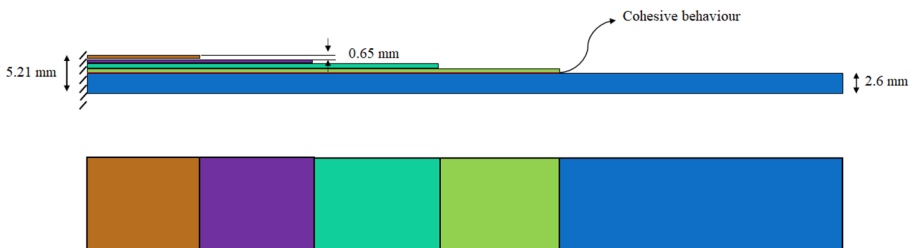

Fig. 13 Specimen configuration for ply-drop without crack

Table 4 Material property ply-drop configuration

Laminate Property		Interfacial Properties	
E_{11} (GPa)	120	G_{Ic} (N/mm)	0.260
$E_{22} = E_{33}$ (GPa)	10.5	G_{IIc} (N/mm)	1.002
$G_{12} = G_{13}$ (GPa)	5.25	$\sigma_{I, max}$ (MPa)	30
G_{23} (GPa)	3.48	$\sigma_{II, max}$ (MPa)	60
$\nu_{12} = \nu_{13}$	0.3	K_I (N/mm^3)	10^6
ν_{23}	0.5	K_{II} (N/mm^3)	10^6

Since no analytical or experimental results are available in the literature for the comparison, the present results are compared with VCCT analysis as it is independent of any input parameters. Similar to the MMB result, it can be observed in Fig. 14 that the elements size less than 1 mm were able to give assenting results. It can be observed from Fig. 15 that in contrast to MMB simulations, higher or more pragmatic interfacial stress is preferred in ply-drop. The sharp prediction of load with lower values of interfacial stress can be associated with the presence of a larger process zone resulting in larger energy absorption. However, the higher values of interfacial stresses tend to give more consistent results. It is due to a small fracture process zone wherein the process in mode-I dominates at the initial stage and mode-II at the end. This can also be justified by a sudden drop in peak load with an unequal variation of interfacial stress (30 MPa, 90 MPa), as shown in Fig. 15. Therefore, for the prediction of LCZ, a mode ratio of 20% close to mode-I behavior, interfacial strength of (60 MPa, 90 MPa), and thickness h equal to 2.5 mm is adopted. In case of
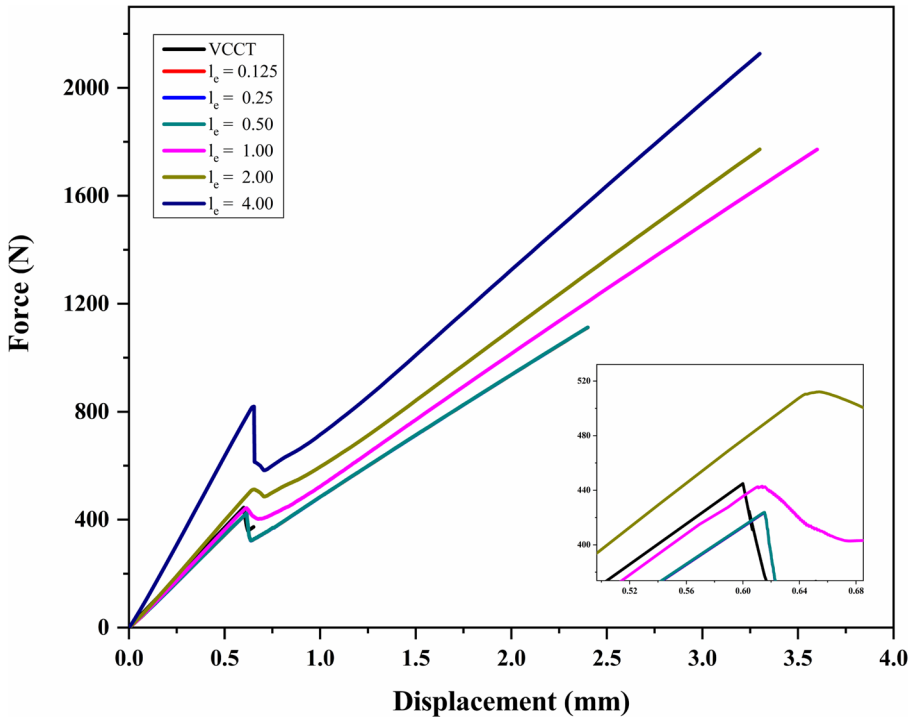

Fig. 14 Effect of element size on load vs. displacement behavior for ply-drop without crack
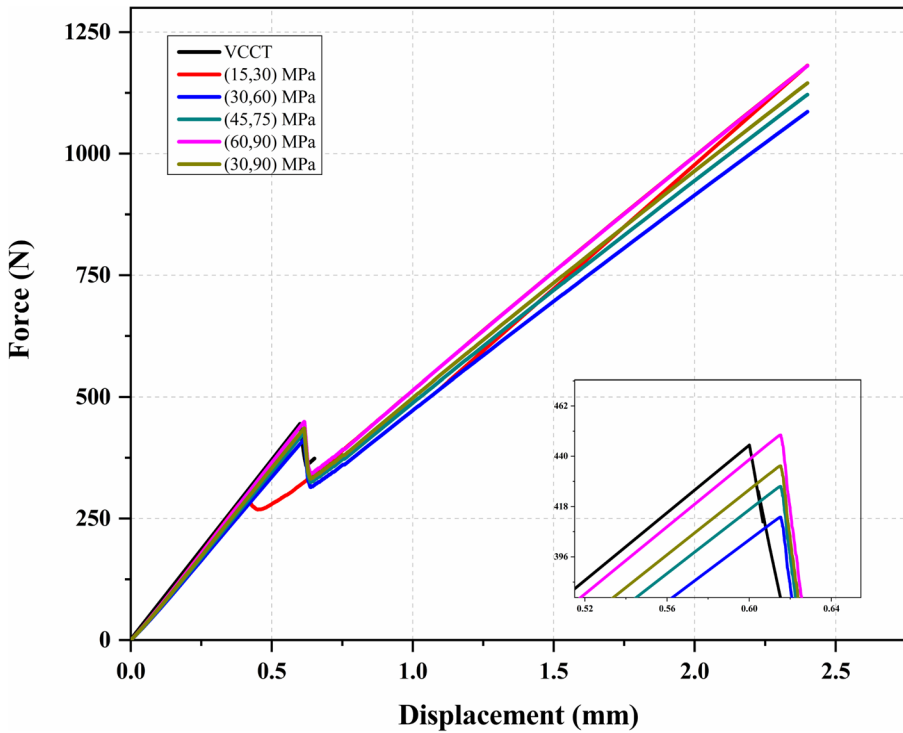
Fig. 15 Effect of interfacial stress on load vs. displacement behavior for ply-drop without crack

ply-drop specimen with material property as in Table 4 and the fit parameters ($h^1 = 2.5483$, $M^0 = 0.7866$, $M^\infty = 0.8950$, m = 0.052801), the LCZ predicted by Eq. 26 is 0.7762 mm, whereas the numerically determined length with mesh size 0.2 mm is 0.7981 mm. The curve fit parameters are obtained based on the least square fit method. Thus, the simulation requires a minimum of 3 or more elements, and the failure process is observed to be strength sensitive.

4.3 Structural Component: Ply-drop with Pre-crack

In this section, another ply-drop with a slightly different configuration subjected to mixed-mode loading is analyzed. The composite laminates are manufactured by stacking laminae with variations in orientation to attain the necessary strength and stiffness. Thus, it
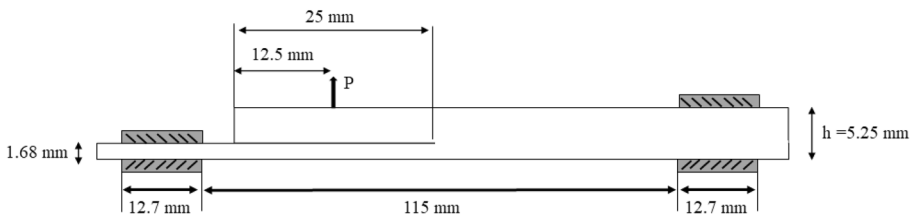

Fig. 16 Ply-drop configuration specimen with crack

Table 5 Material property for ply-drop with crack

Laminate Property		Interfacial Properties	
E_{11} (GPa)	161	G_{Ic} (N/mm)	0.210
$E_{22}=E_{33}$ (GPa)	11.38	G_{IIc} (N/mm)	0.770
$G_{12}=G_{13}$ (GPa)	5.17	$\sigma_{I,\,max}$ (MPa)	60
G_{23} (GPa)	3.98	$\sigma_{II,\,max}$ (MPa)	90
$\nu_{12}=\nu_{13}$	0.32	K_I (N/mm^3)	10^6
ν_{23}	0.44	K_{II} (N/mm^3)	10^6

becomes a provenance of complex out-of-plane stresses leading to initiation of failure. A structural specimen [55], as shown in Fig. 16, with cross-ply orientation is investigated. The ply-drop specimen of a total thickness of 5.29 mm with 44 layers and thickness of each layer equal to 0.12 mm is considered. The stacking sequence of the ply-drop specimen considered is $[0_4/90_{12}/0_{10}90_4/\mathbf{T}/0/90/0_2/90_6/0_2/90/0]$, where T depicts the initial crack. The specimen is modeled with plane strain elements, and the material properties considered are listed in Table 5. The cohesive behavior is defined at a ply-drop between two plies of different orientations with a pre-crack of 25 mm. The effect of element size and interfacial strength on the load–displacement behavior is investigated. The element size is varied in the scale of 0.125 mm to 4 mm, and interfacial strength is diverse in the scale (15 MPa $\leq$ Mode-I $\leq$ 60 MPa; 30 MPa $\leq$ Mode-II $\leq$ 120 MPa).
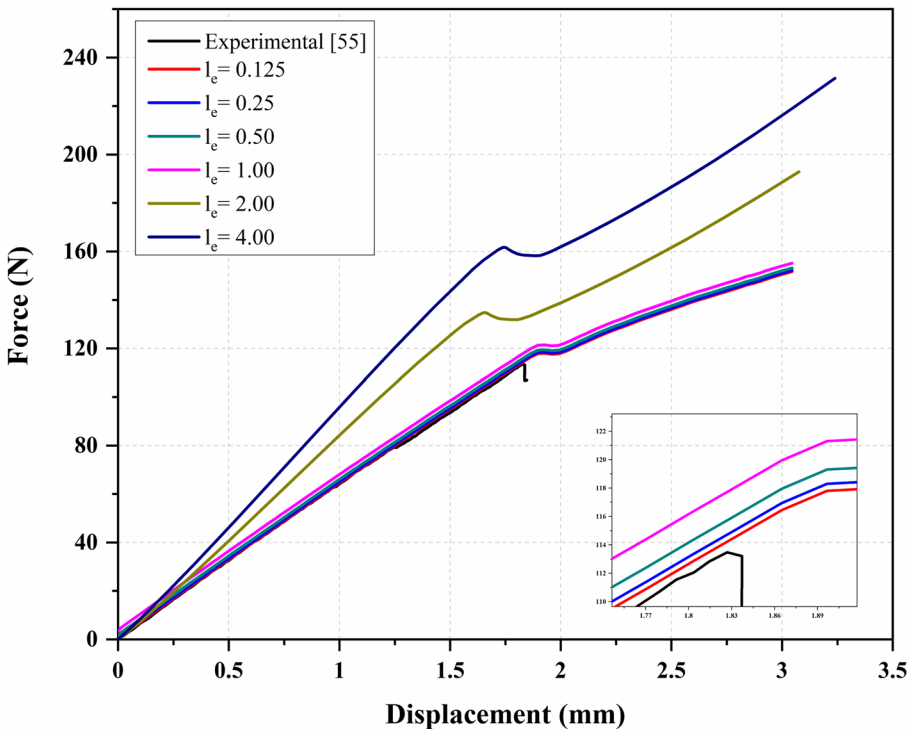

Fig. 17 Effect of element size on load vs. displacement behavior for ply-drop with crack
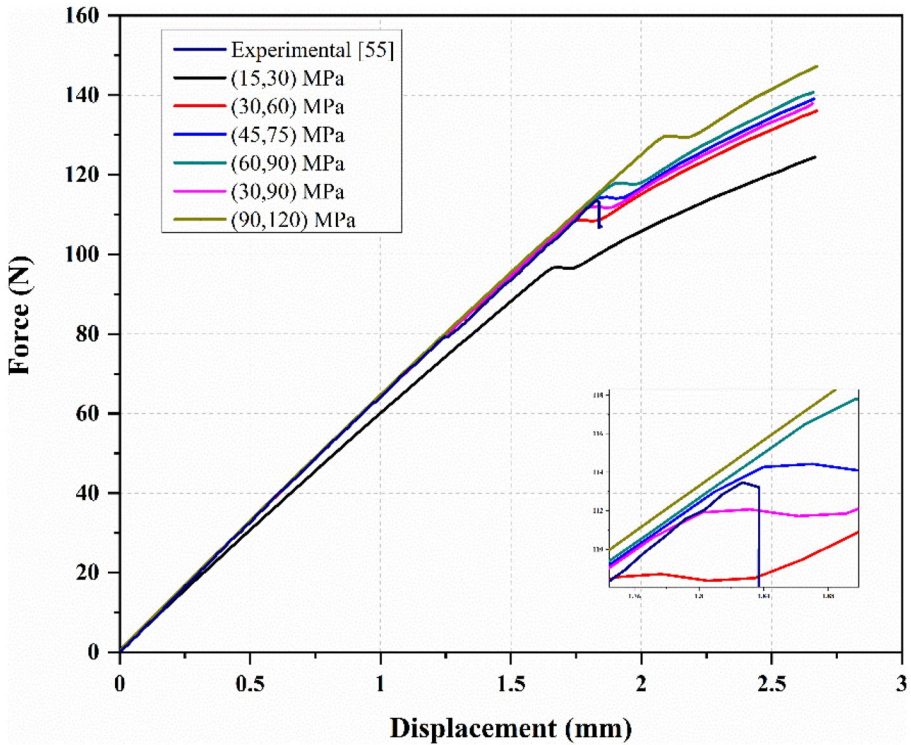
Fig. 18 Effect of interfacial stress on load vs. displacement behavior for ply-drop with crack

A similar trend of the load–displacement behavior can be observed with variations of element size, as shown in Fig. 17. The element size greater than 1 mm are insufficient and overestimate the peak load as well as softening behavior. It can be noted that the element size smaller or near to 1 mm exhibits a close match to experimental results. However, accurate prediction of the curve is possible with an element size of 0.5 mm or less.

It can be noticed from Fig. 18 that with the increment in interfacial strength, the values close to material property give accurate load–displacement behavior. The interfacial values of 60 MPa and 90 MPa are observed to give a higher prediction of peak stress than the experimental curve. This variation in the curves can be attributed to the load drop due to crack migration or shift around 80 MPa. The peak value predicted drops to a lower value with the variation of interfacial strengths from (60 MPa, 90 MPa) to (30 MPa, 90 MPa), which shows mode-I dominant failure [36]. For interfacial strength values, mode-II > 90 MPa and mode-I < 30 MPa are insufficient to estimate the result. As depicted in Fig. 17, it results in either under prediction (15 MPa, 30 MPa) or over prediction (90 MPa,120 MPa) of the load–displacement relation. In order to predict LCZ, the mixed-mode ratio is assumed to be 20%, and the thickness h is considered to be 2.65 mm. The LCZ as estimated by Eq. (26) is 0.4940 mm (h^1 = 2.4950, M^o = 0.5212, M^∞ = 0.538276, m = 0.020877) and numerical value obtained with element size of 0.125 mm is equal to 0.5214 mm. Accordingly, a minimum number of four elements are required in the cohesive zone to predict the behavior accurately [48].
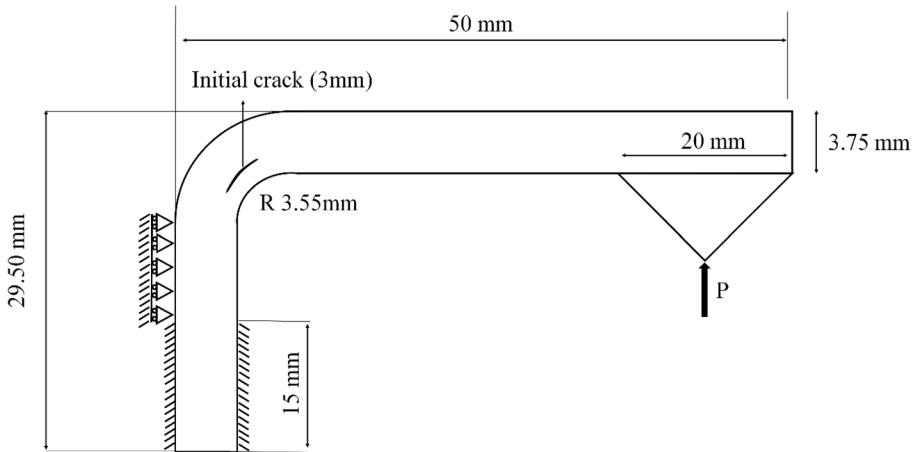
Fig. 19 L bend configuration specimen with crack

4.4 Structural Component: L Bend

Curved composite structures form an integral part of many engineering applications, such as defence, aerospace, automotive, and medical devices. Often, in the aerospace industry, for components like wing spars or to connect any parallel/ orthogonal panels, L-shaped curved composites structures have been used. These structures are often subjected to complex loads such as bending and out-of-plane stresses, making them a weak zone in the complete system. Besides, the stacking of lamina and the alignment of fibers concocts to a failure behavior even more complex leading to unstable delamination and global failure of the assembly. Therefore, to predict the failure in such components, an L-shaped laminated composite (L-bend) [56] is modeled, as shown in Fig. 19. The numerical model consists of a total thickness of 3.75 mm with the stacking sequence $[0_3/90_3/0_3/\mathbf{T}/90_3/0_6/90_3/0_3/90_3/0_3]$, where T depicts the initial crack of 3 mm.

The plane strain elements were used to model the L bend specimen with the properties given in Table 6. In between the ninth 0º ply and the tenth 90º ply, the cohesive contact behavior was defined with the initial crack, as shown in Fig. 19. The load–displacement behavior of the structure is investigated for variation in element size of 0.125 mm to 4 mm and interfacial strength ranging from 15 MPa $\leq$ Mode-I $\leq$ 60 MPa; 30 MPa $\leq$ Mode-II $\leq$ 120 MPa.

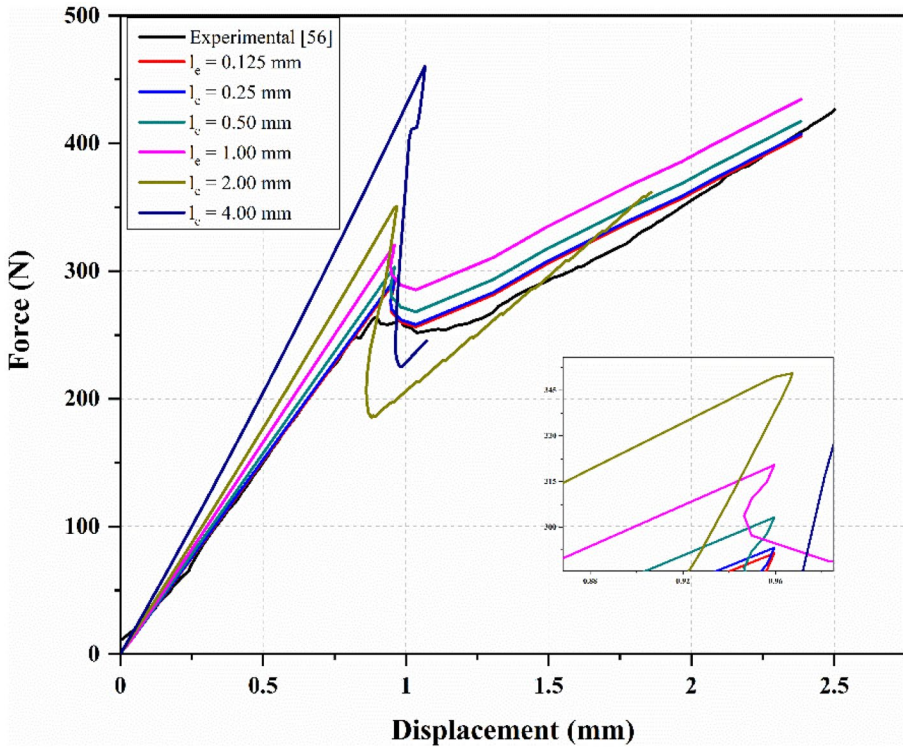| Table 6 Material property for L bend configuration	Laminate Property		Interfacial Properties	
	E_{11} (GPa)	133	G_{Ic} (N/mm)	0.133
	$E_{22}=E_{33}$ (GPa)	9	G_{IIc} (N/mm)	0.4588
	$G_{12}=G_{13}$ (GPa)	4.4	$\sigma_{I,\,max}$ (MPa)	60
	G_{23} (GPa)	3.7	$\sigma_{II,\,max}$ (MPa)	80
	$\nu_{12}=\nu_{13}$	0.35	K_I (N/mm^3)	10^6
	ν_{23}	0.2857	η	1

Fig. 20 Effect of element size on load vs. displacement behavior for L bend

It can be observed from Fig. 20 that the element size equal to or less than 0.5 mm are sufficiently capable of predicting load–displacement relation. The element size greater than 1 mm significantly overestimates peak load and does not capture exact softening behavior. With the variation in interfacial stress, it can be witnessed from Fig. 21 that the load–displacement behavior with the stress values close to the actual material properties exhibits good agreement with the experimental results. Like ply-drop configuration, L bend is also subjected to crack shift/migration, resulting in a higher prediction of load with interfacial stress of (60 MPa, 80 MPa). Also, the strength values higher than (60 MPa, 90 MPa) and lower than (15 MPa, 30 MPa) are unsustainable in estimating the result. The values either under predict (15 MPa, 30 MPa) or over-predict (90 MPa, 120 MPa) the peak load value. To check the mode dominancy, the value of stress was decreased to (30 MPa, 90 MPa). A sudden drop in the predicted peak value of the load is observed, depicting mode-I dominant delamination [57]. Thus, it can be ascertained that L bend delamination is strength sensitive. To calculate LCZ, the specimen is meshed with coarse mesh on one end and fine mesh on the other end of the initial crack to allow crack initiation at one end only [58]. The LCZ is calculated based on Eq. (26) with h=1.875 mm and an element size of 0.05 mm. The LCZ predicted by the Eq. 26 is 0.2321 mm, while the numerical value obtained is equal to 0.2100 mm. The fit parameters (h^1=2.4950, M^0=0.5212, M^∞=0.538276, m=0.020877) were obtained using least square method. Thus, a fine mesh with a minimum of 4 or more elements is required to capture load–displacement behavior.
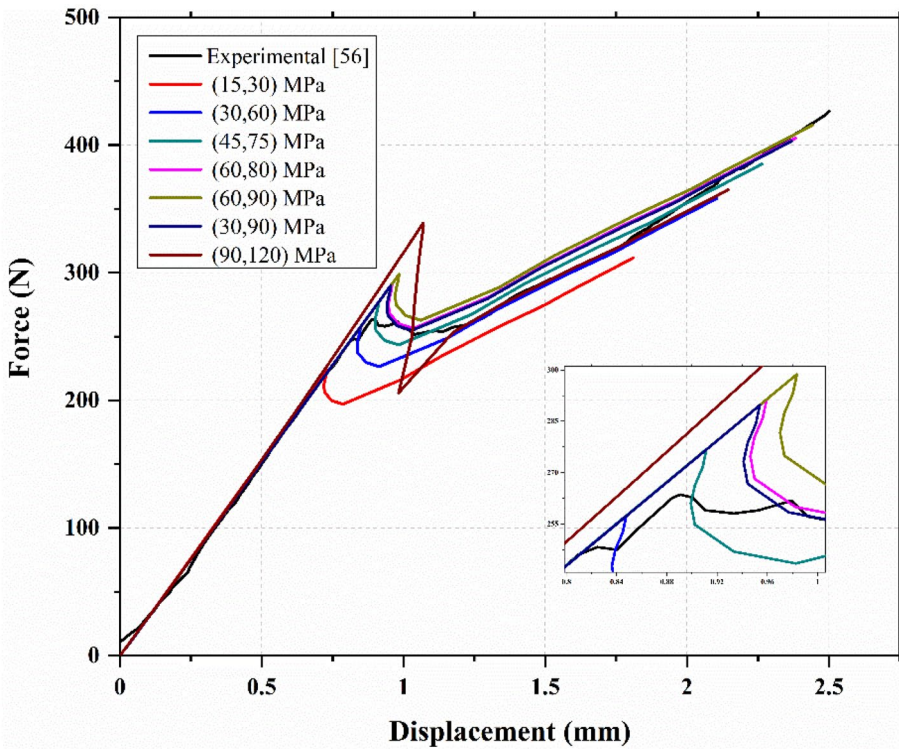
Fig. 21 Effect of interfacial stress on load vs. displacement behavior for L bend

5 Crack Migration

The composite structural failure in many cases is dominated by delamination. However, it is consistently accompanied by matrix or fiber failure leading to multiple delaminations or cracks. This delamination often propagates and shift into other lamina interfaces resulting in the crack shift or delamination migration, as shown in Fig. 22. Similar behavior has been recorded in many experimental studies [59–62] as well as in the studies carried out in the previous section. It can be noticed from the load–displacement behavior of both the ply-drop with initial crack (Fig. 18) and L-bend (Fig. 21) that the load predicted is slightly higher than that of the experimental results. It can be attributed to the premature matrix cracking and crack shift/migration occurring at 0°/90° lamina interfaces of both the structures. As He and Hutchinson [63] defined, the crack shift into the adjacent lamina is ascribed as 'kinking', and the migration is referred to complete process of delamination propagation to another lamina interface. The current section focuses on modeling the crack kinks and delamination migration to accurately predict load–displacement behavior. A Modified Embedded Cohesive Model (MECM) approach is proposed to predict crack kinking and migration to estimate the behavior.
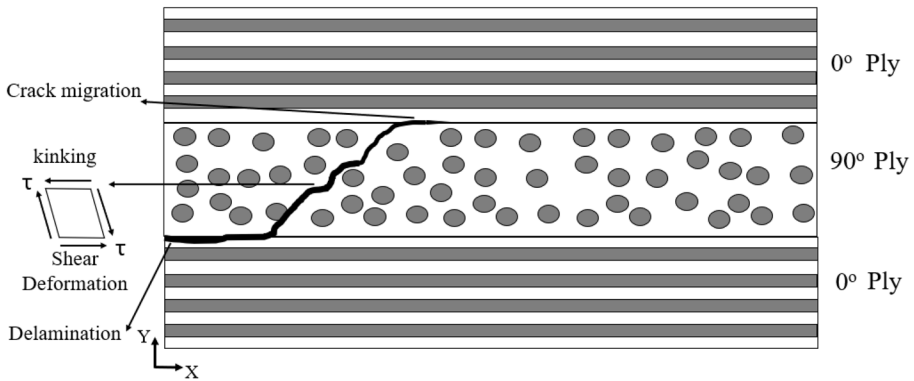
Fig. 22 Representation of crack/delamination migration due to initiation of transverse matrix crack

5.1 Model Description

The proposed model is an improvisation over Needleman's [64] intrinsic cohesive behavior model wherein cohesive interaction is established in between elements. The finite element discretization is based on the estimation of crack propagation along the specific path that consists of cohesive zone surfaces. Thus, representing the actual behavior of delamination propagation. The discretization in the current model is contingent on the brick and mortar model proposed by Begley et al. [65]. They investigated the behavior of nacre-influenced material topologies. The model allows assigning of the material property that is independent of orientations. A similar approach is followed in the current study to model unidirectional composite material structures. The present research is focused on modeling 0º/90º cross-ply laminate structures where material property depends on the fiber orientation. In comparison with Begley's model [65], the current method represents a solid element as brick and cohesive behavior as mortar, as shown in Fig. 23. The model allows predicting both intralaminar matrix failure (matrix cracking/kinking) as well as interlaminar matrix failure (delamination).
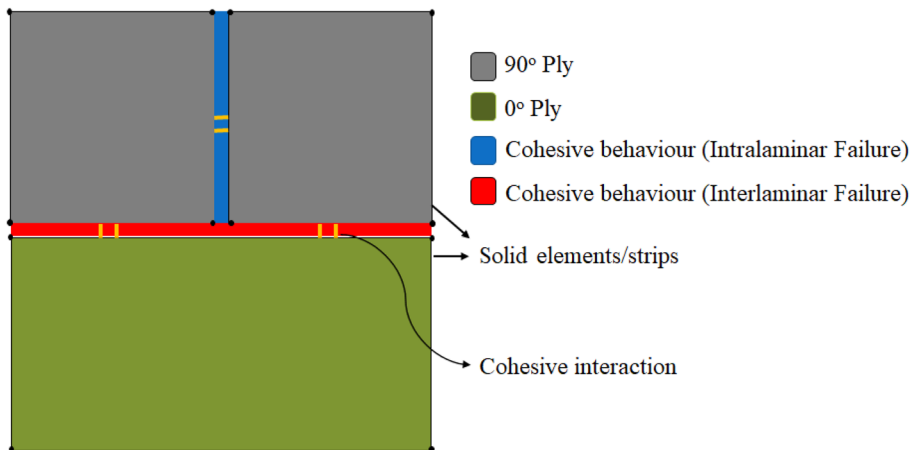

Fig. 23 Schematic representation of the Modified Embedded Cohesive Model (MECM) approach applied to unidirectional composite

The cohesive behavior is inserted between solid elements representing unidirectional plies in a different orientation. The vertical interaction depicts the intralaminar, and the horizontal interaction illustrates the interlaminar matrix failure. The model assumes that the matrix cracks are approximated to be vertical.

Furthermore, a simple beam with cross-ply orientation is considered to extend the approach further to structure, as shown in Fig. 24. The blue colour depicts the matrix cracks, and the red colour represents the delamination. Introducing several cohesive behaviors among the elements introduces the problem of artificial compliance to the model and largely influences the total behavior of the structure. The widely used approach to overcome this problem is to increase the initial stiffness of cohesive behaviour. However, this would require higher computational time leading to expensive simulation. Hence, in the current numerical model, the discretization to define cohesive behavior is limited to regions with 90° plies where the failure is inevitable, as shown in Figs. 23 and 24. The 0° plies are modeled for interlaminar delamination only. Also, the element's size is a factor that is inversely proportional to artificial compliance [16, 66]. As a result, brittle materials like polymer composites require small element size (l_e) as a consequence of a smaller fracture process zone or cohesive length. Hence, to establish the convergence in simulation, the association between length scales must be defined.

The model requires the definition of three main length scales, mainly specimen dimension (h), the length of the cohesive zone (l_{cz}), and the length of each element (l_e). The cohesive zone's length depends on maximum traction, fracture energy, and elastic modulus of the material. The estimation of LCZ is made based on Eq. (26) for mixed-mode. The length of the element should be less than LCZ ($l_e < l_{cz}$) to provide accurate solutions [38]. The bilinear cohesive surface behavior which is more robust as compared to other traction separation law is utilized. The proposed methodology is validated for the ply-drop with initial crack and L bend configurations in the next section.

5.2 Ply-drop

The basic configuration of the investigated structural specimen is shown in Fig. 16, similar to the one analyzed in Sect. 4.3. The material properties and boundary conditions are also maintained identical. The load–displacement behavior shows a variation in peak load predictions, as shown in Fig. 18. The experimental observations made by Ratcliffe et al.
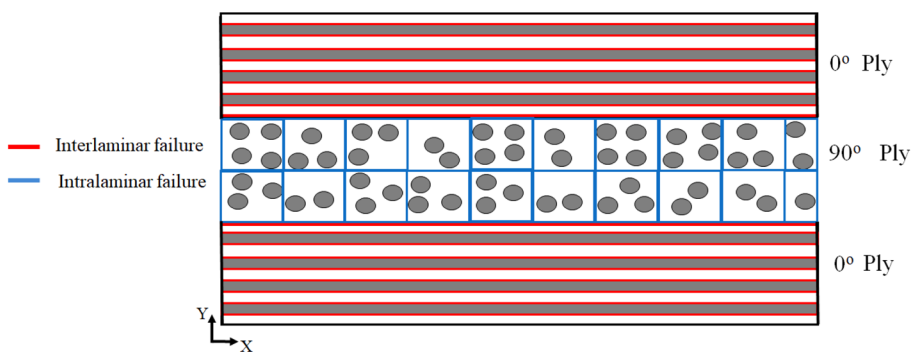

Fig. 24 Schematic representation of cross-ply laminate modeled with improved embedded cohesive zone model

[55] demonstrated the intralaminar matrix failure with the occurrence of crack kinking at 0º/90º interface and subsequently leading to the migration of the crack to another ply. For the modeling of such a phenomenon, the MECM approach is utilized. The discretization is made to 90-degree ply orientation only, and the element size was decided based on the LCZ calculated using Eq. (26). The discretization and element size were maintained less than LCZ to keep a minimum number of elements in the process zone to accurately capture failure. This also ensures convergence and reduces artificial compliance problems. The ply-drop configuration has a total thickness of 5.29 mm and a total of 44 plies with 0º and 90º orientations. The discretization was generated for each ply with a thickness of 0.12 mm. The discretization of the model is set up by a user-defined python script within the framework of Abaqus pre-processor. The model is built ply-by-ply, starting from the bottom. The mesh is generated for each ply, and the discretization is carried out only for 90º plies where the matrix cracking is anticipated. The size of each discretization strip is based on the total length of the cohesive zone.

As calculated in Sect. 4.3, for the model, the length of the cohesive zone is 0.49 mm. Thus, to ensure a minimum of four elements, the length of each element (l_e) is chosen to be 0.12 mm. Thus, each discretized strip is considered in a square shape with a dimension of 0.12 mm on each side, as shown in Fig. 25. The cohesive behavior is defined between the adjacent discretized strips to form a network. The plies with 0º orientation are not expected to exhibit any intralaminar failure. Therefore, only interlaminar failure leading to delamination is defined in between the plies. The blue line indicates the cohesive behavior for matrix failure, whereas the red line indicates cohesive behavior for delamination. The process is replicated for every ply based on the orientation of the configuration of the ply-drop until the complete model is achieved. Consequently, this leads to a network of the embedded cohesive zone allowing to capture both interlaminar matrix failure in 90º ply and intralaminar delamination in 0º ply.

It can be seen from Fig. 26 that the crack migration is observed from the plane of the initial pre-crack. Similar experimental behavior was observed [55] at loading position L = 0.5a. It can be attributed to the shear stresses acting at the vicinity of the initial crack tip, which results in crack kinking due to matrix failure across the 90º ply stacking orientation. The behavior is due to the failure of cohesive surfaces along the discretized strips. As the damage propagation reaches 0º/90º interface, the crack starts to propagate as interlaminar delamination leading to migration of crack. As the matrix cracking occurs due to kinking, and the migration progress to another interface, a load drop is noticed. The estimated
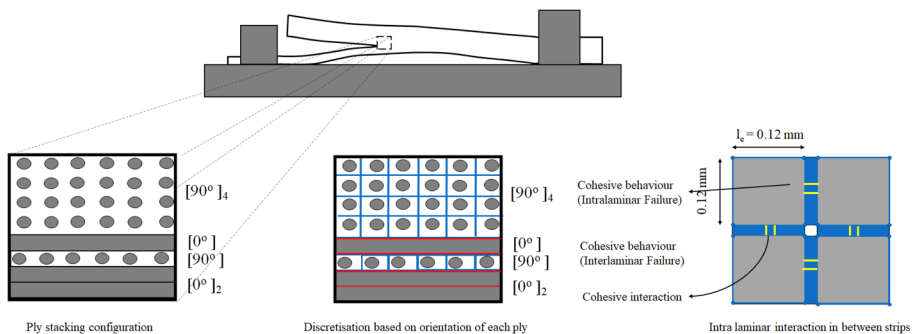

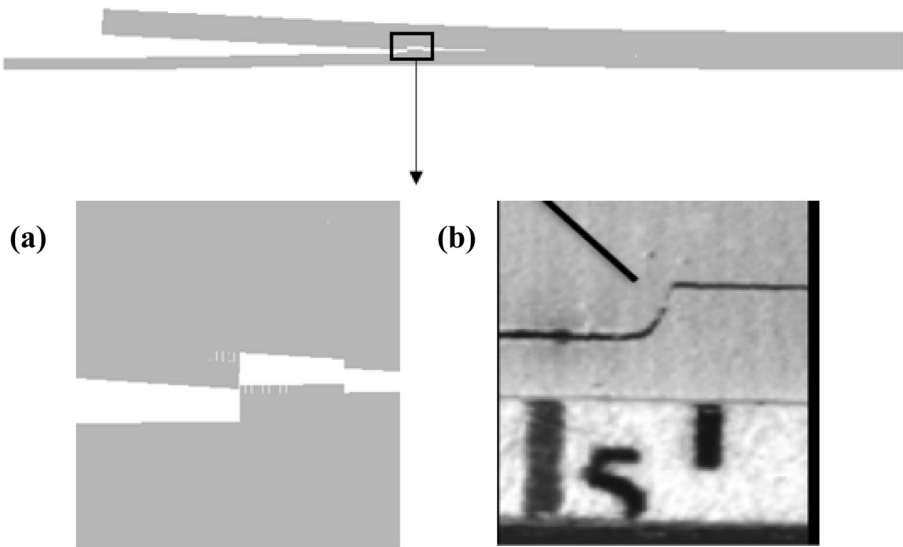**Fig. 25** Numerical model discretization representation for ply-drop

Fig. 26 Comparison of numerical (MECM) and experimental crack kink, delamination pattern for ply-drop with initial crack; (**a**) MECM, (**b**) Experimental [55]

load–displacement behavior as compared to experimental results is in good agreement, as shown in Fig. 27. However, there is a slightly higher prediction of peak load, which can be associated with the rigid behavior of the model as a consequence of the increase in stiffness [16]. The load drop predicted numerically is approximately equal to 81 N, which is close to the experimental value. The migration pattern is similar to the experimental, as shown in Fig. 27, thus capturing failure more precisely.

5.3 L Bend

Failure in curved composites structures is mainly due to complex damage progression, which is often accompanied by intralaminar matrix failure and interlaminar delaminations. A similar structural composite with the L shape component discussed in earlier Sect. 4.4 is analyzed for crack migration and matrix cracking. It can be observed in Fig. 21 that the load–displacement behavior is overpredicting the peak load values as compared to that of experimental results. It can be accredited to matrix cracking leading to crack kinks and delamination migration in the structure that can be observed in an experimental study [56]. To precisely estimate the behavior and to simulate crack kinks, a modified embedded cohesive zone approach is used. An approach similar to the modeling of ply-drop specimen configuration is implemented. The L bend has a total thickness of 3.75 mm, and each lamina of about 0.125 mm thick. The model is established ply by ply using python script for Abaqus pre-processor. The LCZ, as calculated by Eq. (26), is equal to 0.23 mm, whereas the numerically obtained value is equal to 0.21 mm. The plies with 90° orientation are discretized based on LCZ obtained. Since the process zone size comparably small, the numerical model would require an enormous number of discretized strips and cohesive interactions to be defined. This would contribute to an increase in artificial stiffness, causing convergence issues. Therefore, to avoid this computational problem, the length of each
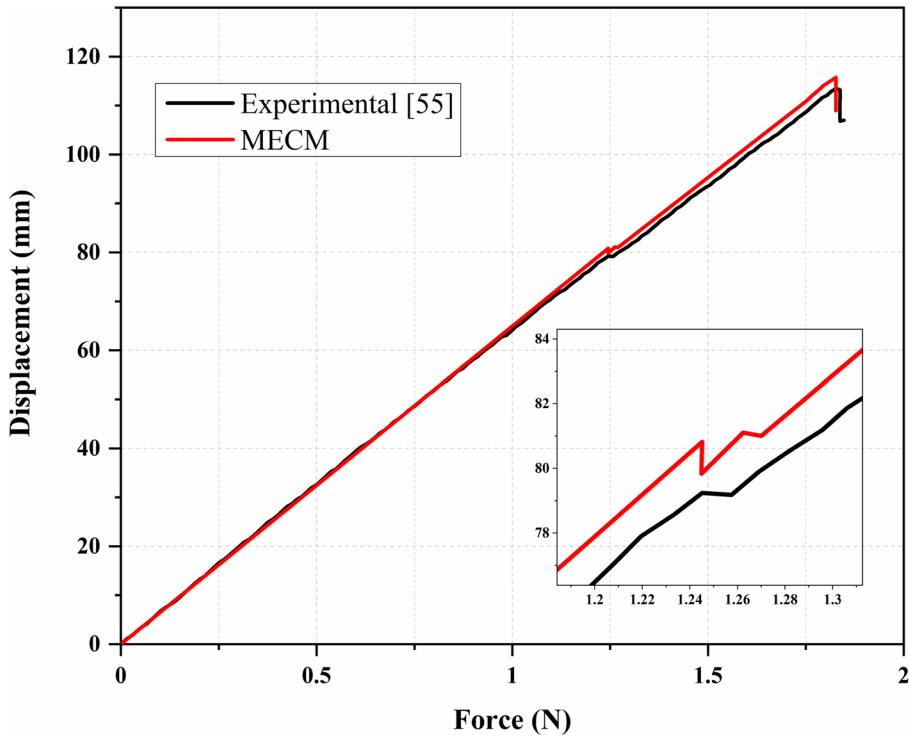
Fig. 27 Comparison of Predicted (MECM) and measured [55] force vs. displacement behavior for ply-drop with initial crack

discretized strip is considered equivalent to the estimated LCZ by Eq. (26). Each discretized strip is meshed with four elements to maintain a minimum number of elements in the process zone. The size of each strip was assumed to be equal to 0.125 mm to ensure uniformity, and the element size, l_e equal to 0.031 mm, as shown in Fig. 28. It resulted in reduced artificial compliance, and thus convergence in the solution is obtained. The cohesive behavior for intralaminar failures depicting matrix failure is inserted in between two strip surfaces. The 0° are assigned with interlaminar cohesive behavior, as plies are not expected to have any intralaminar failures. The load and the material property are the same as that of the model discussed in Sect. 4.4.

The failures obtained from numerical results, as shown in Fig. 29, exhibit matrix dominate failure in 90° piles. The initial kinking is followed by delamination with crack migration to 0°/90° interface. With the further increase in the load, multiple matrix failure with crack kinking is observed, followed by delamination along with the different 0°/90° interface. The predicted and measured load–displacement curves are in close agreement, as shown in Fig. 30. The load at which the kinking occurs is marginally more due to the initial rigidity of the structure. The proposed methodology using the Modified Embedded Cohesive Zone Model (MECM) approach can relatively predict both intralaminar and interlaminar failures in curved composites under mixed-mode loading.
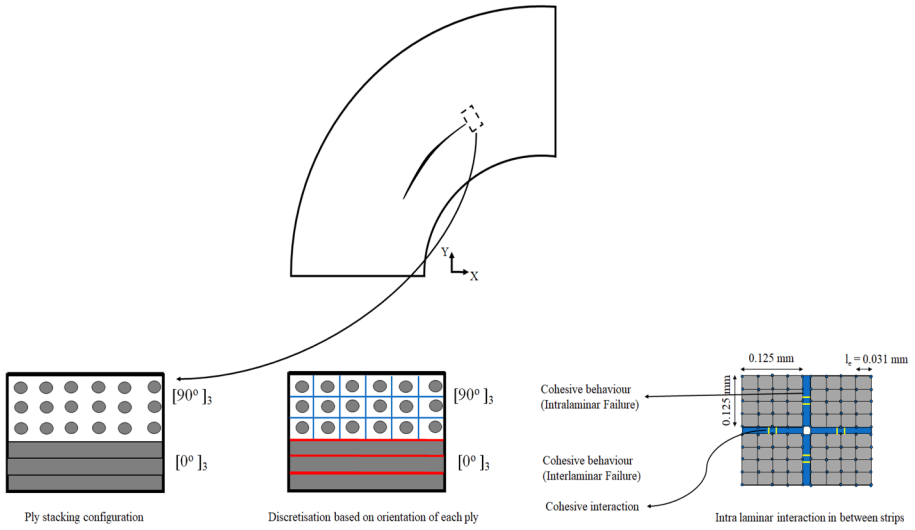
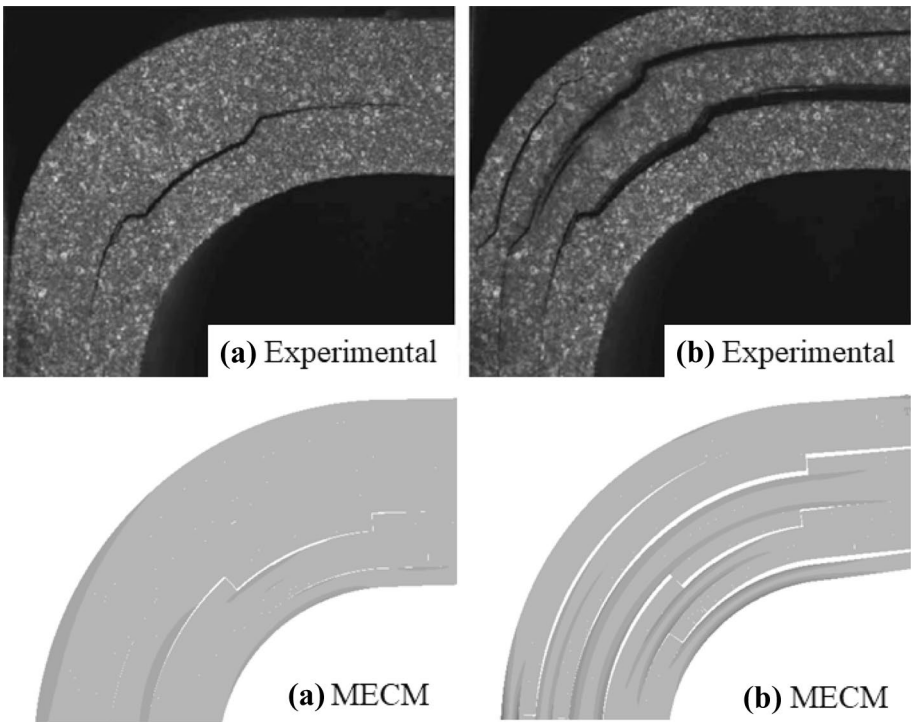**Fig. 28** Numerical model discretization representation for ply-drop

Fig. 29 Comparison of numerical (MECM) and experimental [56] crack kink and delamination pattern for L-bend; (**a**) at 2 mm load level, (**b**) 7 mm load level
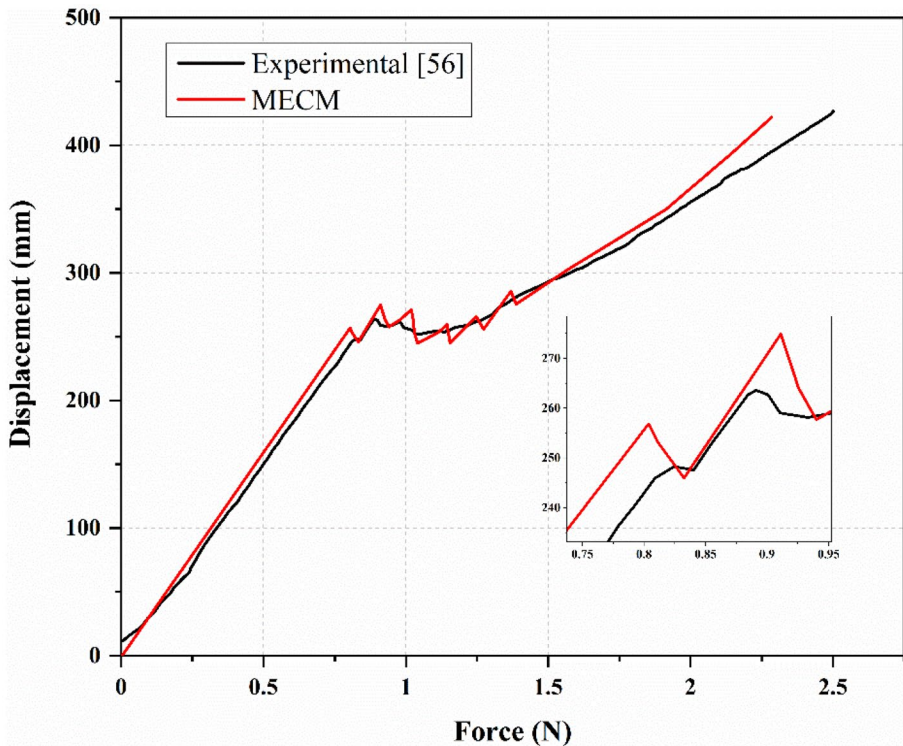
Fig. 30 Comparison of Predicted (MECM) and measured [56] force vs. displacement behavior for L bend

6 Conclusions

Based on the numerical investigations, a novel empirical expression is proposed for mixed-mode loading delamination. A fairly good agreement was observed between the numerical and predicted values of LCZ for various structural configurations. The influence of input parameters such as interfacial stress and element size on load–displacement behavior was also investigated. It was noticed that for simple specimen configurations, like MMB, accurate prediction of behavior could be achieved with a wide range of interfacial stress values. However, for the complex geometries like ply-drop or L-bend, the values close to actual material properties provided accurate predictions. A precise estimation of behavior can be obtained with shorter LCZ with values close to the true strength of the material. Hence, it requires a minimum of three to four elements in the cohesive zone for the prediction. Further, a Modified Embedded Cohesive Model was proposed to investigate the intralaminar matrix cracking and interlaminar delamination. The numerical investigations revealed that the failure in composites is accompanied by simultaneous multiple crack initiation and propagation. Bsides, the intralaminar cracks and interlaminar delamination combined to form a crack kinks and delamination migrations, as observed in the experimental studies. It is observed that the numerical and experimental results exhibit excellent agreement with reduced computational efforts. Therefore, the proposed methodology can be used to predict the LCZ and various failures such as intralaminar and interlaminar failures in composites of various geometries under mixed-mode loading.

Appendix 1

Equivalent Elastic Modulus

For orthotropic materials equivalent elastic modulus, E_I' and E_{II}' are calculated as

$$E_I' = \left(\frac{a_{11}a_{22}}{2}\right)^{-\frac{1}{2}} \left[\left(\frac{a_{22}}{a_{11}}\right)^{\frac{1}{2}} + \frac{2a_{12} + a_{66}}{2a_{11}}\right]^{-\frac{1}{2}} \tag{29}$$

$$E_{II}' = \left(\frac{a_{11}}{\sqrt{2}}\right)^{-1} \left[\left(\frac{a_{22}}{a_{11}}\right)^{\frac{1}{2}} + \frac{2a_{12} + a_{66}}{2a_{11}}\right]^{-\frac{1}{2}} \tag{30}$$

where, a_{11}, a_{22}, a_{12} and a_{66} under plane stress condition are given by

$$a_{11} = \frac{1}{E_{11}}$$
$$a_{22} = \frac{1}{E_{22}}$$
$$a_{12} = -\frac{v_{12}}{E_{22}}$$
$$a_{66} = \frac{1}{G_{12}}$$

For plane strain condition, the equivalent elastic modulus is given by

$$E_I' = \left(\frac{E_{22}}{Q}\right) \tag{31}$$

$$E_I' = \left(\frac{E_{22}}{Q}\right) \left(\frac{E_{11}}{E_{22}}\right)^{\frac{1}{2}} \tag{32}$$

where,

$$Q = \frac{1}{2}\sqrt{2\left[\left(\frac{E_{11}}{E_{22}}\right)^{\frac{1}{2}} - v_{21}\right] + \frac{E_{11}}{G_{12}}} \tag{33}$$

Variables under plane strain condition

$$a_{11} = \frac{1}{E_{11}} - \frac{v_{31}^2}{E_{33}}$$
$$a_{22} = \frac{1}{E_{22}} - \frac{v_{32}^2}{E_{33}}$$
$$a_{12} = -\frac{v_{12}}{E_{22}} - \frac{v_{31}v_{32}}{E_{33}}$$
$$a_{66} = \frac{1}{G_{12}}$$

Appendix 2

Analytical (LEFM) Load–displacement Relation for MMB Test

The load–displacement behavior for MMB can be obtained as per ASTM standard D5528. The applied load and displacement relation are obtained by

$$F_{arm} = \sqrt{\frac{G_c}{\frac{4(3c-L)^2(a+\xi h)^2+3(c+L)^2(a+0.42\xi h)^2}{64bL^2\frac{E_{11}bh^3}{12}}}} \qquad (34)$$

where, ξ is given by

$$\xi = \sqrt{\frac{E_{11}\left[3 - 2\left(\frac{g}{1+g}\right)^2\right]}{11G_{13}}}$$

$$g = 1.18\frac{\sqrt{E_{11}E_{22}}}{G_{13}}$$

The corresponding arm displacement is given by

$$U_{arm} = F_{arm}\frac{4(3c - L)^2(a + \xi h)^3 + (c + L)^2\left[3(a + 0.42\xi h)^3 + 2L^3\right]}{96L^2\frac{E_{11}bh^3}{12}} \qquad (35)$$

Authors Contributions All the authors contributed to the study conceptualization. The methodology, formal analysis and investigation and writing of original draft were performed by Chetan H. C. The required fund acquisition, resources, supervision of research, review and editing the article were performed by Dr. Subhaschandra Kattimani and Prof. S. M. Murigendrappa.

Declarations

Conflict of Interest The authors have no conflicts of interest to declare that are relevant to the content of the article.

References

1. Wang, Y., Soutis, C.: Fatigue Behaviour of Composite T-Joints in Wind Turbine Blade Applications. Appl. Compos. Mater. **24**, 461–475 (2017). https://doi.org/10.1007/s10443-016-9537-9
2. Suman, M.L.J., Murigendrappa, S.M., Kattimani, S.: Effect of similar and sissimilar interface layers on delamination in hybrid plain woven glass/carbon expoxy laminated compoiste double cantilever beam under model-I loading. Theor. Appl. Fract. Mech. **114**, 102988 (2021). https://doi.org/10.1016/j.tafmec.2021.102988
3. Dugdale, D.S.: Yeilding of steel sheets contaning slits. J. Mech. Phys. Solids **8**, 100–104 (1906). https://doi.org/10.1016/0022-5096(60)90013-2
4. Barenblatt, G.I.: The Mathematical Theory of Equilibrium Cracks in Brittle Fracture. Adv. Appl. Mech. **7**, 55–129 (1962). https://doi.org/10.1016/S0065-2156(08)70121-2
5. Alfano, G.: On the influence of the shape of the interface law on the application of cohesive-zone models. Combust. Sci. Technol. **66**, 723–730 (2006). https://doi.org/10.1016/j.compscitech.2004.12.024
6. Azab, M., Parry, G., Estevez, R.: An analytical model for DCB/wedge tests based on Timoshenko beam kinematics for accurate determination of cohesive zone lengths. Int. J. Fract. **222**, 137–153 (2020). https://doi.org/10.1007/s10704-020-00438-2
7. Soto, A., González, E.V., Maimí, P., Turon, A., Sainz de Aja, J.R., de la Escalera, F.M.: Cohesive zone length of orthotropic materials undergoing delamination. Eng. Fract. Mech. **159**, 174–188 (2016). https://doi.org/10.1016/j.engfracmech.2016.03.033
8. Esmaili, A., Fathollah Taheri-behrooz.: Effect of cohesive zone length on the delamination growth of the composite laminates under cyclic loading. Eng. Fract. Mech. **237**, 107246 (2020). https://doi.org/10.1016/j.engfracmech.2020.107246
9. Naderi, M., Jung, J., Yang, Q.D.: A three dimensional augmented finite element for modeling arbitrary cracking in solids. Int. J. Fract. **197**, 147–168 (2016). https://doi.org/10.1007/s10704-016-0072-3
10. Pinho, S.T., Chen, B.Y., De Carvalho, N.V., Baiz, P.M., Tay, T.E.: A floating node method for the modelling of discontinuities within a finite element. ICCM Int. Conf. Compos. Mater. **19**, 516–527 (2013)
11. Rabczuk, T., Bordas, S., Zi, G.: On three-dimensional modelling of crack growth using partition of unity methods. Comput. Struct. **88**, 1391–1411 (2010). https://doi.org/10.1016/j.compstruc.2008.08.010
12. Köllner, A., Kashtalyan, M., Guz, I., Völlmecke, C.: International Journal of Solids and Structures On the interaction of delamination buckling and damage growth in cross-ply laminates. **202**, 912–928 (2020). https://doi.org/10.1016/j.ijsolstr.2020.05.035
13. Qing, L., Su, Y., Dong, M., Cheng, Y., Li, Y.: Size effect on double-K fracture parameters of concrete based on fracture extreme theory. Arch. Appl. Mech. **91**, 427–442 (2021). https://doi.org/10.1007/s00419-020-01781-5
14. Kashtalyan M., Soutis C.: Damage mechanisms in cross-ply fiber-reinforced composite laminates. Wiley Encycl. Compos., 28–31 (2012). https://doi.org/10.1002/9781118097298.weoc064
15. Tijssens, M.G.A., Sluys, B.L.J., Van der Giessen, E.: Numerical simulation of quasi-brittle fracture using damaging cohesive surfaces. Eur. J. Mech. A/Solids. **19**, 761–779 (2000). https://doi.org/10.1016/S0997-7538(00)00190-X
16. Tabiei, A., Zhang, W.: Cohesive element approach for dynamic crack propagation : Artificial compliance and mesh dependency. Eng. Fract. Mech. **180**, 23–42 (2017). https://doi.org/10.1016/j.engfracmech.2017.05.009
17. Ponnusami, S.A., Turteltaub, S., van der Zwaag, S.: Cohesive-zone modelling of crack nucleation and propagation in particulate composites. Eng. Fract. Mech. **149**, 170–190 (2015). https://doi.org/10.1016/j.engfracmech.2015.09.050
18. Lu, X., Chen, B.Y., Tan, V.B.C., Tay, T.E.: A 3D separable cohesive element for modelling the coupled failure in laminated composite materials. ECCM 2018 - 18th Eur. Conf. Compos. Mater. (2020)
19. Pham, D.C., Cui, X., Lua, J., Zhang, D.: A continuum damage description for a discrete crack modeling approach for delamination migration in composite laminates. AIAA/ASCE/AHS/ASC Struct. Struct. Dyn. Mater. Conf. **2018**, 1–13 (2018). https://doi.org/10.2514/6.2018-1222
20. Varandas, L.F., Arteiro, A., Catalanotti, G., Falzon, B.G.: Micromechanical analysis of interlaminar crack propagation between angled plies in mode I tests. Compos. Struct. **220**, 827–841 (2019). https://doi.org/10.1016/j.compstruct.2019.04.050
21. Bretizman, T.D., Iarve, E.V., Swindeman, M.J., Hoos, K., Mollenhauer, D.H., Hallett, S.R.: Discreet damage modeling in open hole polymer matrix composites. European Conference on Composite Material **15**, 24–28 (2012)
22. Tomar, V., Zhai, J., Zhou, M.: Bounds for element size in a variable stiffness cohesive finite element model. Int. J. Numer. Methods Eng. **61**, 1894–1920 (2004). https://doi.org/10.1002/nme.1138

23. Gutiérrez, M.A., De Borst, R.: Deterministic and stochastic analysis of size effects and damage evolution in quasi-brittle materials. Arch. Appl. Mech. **69**, 655–676 (1999). https://doi.org/10.1007/s004190050249

24. Kumar, D., Roy, R., Kweon, J., Choi, J.: Numerical Modeling of Combined Matrix Cracking and Delamination in Composite Laminates Using Cohesive Elements. Appl. Compos. Mater. 397–419 (2016). https://doi.org/10.1007/s10443-015-9465-0

25. Shi, Y., Pinna, C., Soutis, C.: Interface Cohesive Elements to Model Matrix Crack Evolution in Composite Laminates. Applied Composite Materials **21**, 57–70 (2014). https://doi.org/10.1007/s10443-013-9349-0

26. Cao, D., Duan, Q., Hu, H., Zhong, Y., Li, S.: Computational investigation of both intra-laminar matrix cracking and inter-laminar delamination of curved composite components with cohesive elements. Compos. Struct. **192**, 300–309 (2018). https://doi.org/10.1016/j.compstruct.2018.02.072

27. Xu, X.P., Needleman, A.: Numerical simulations of fast crack growth in brittle solids. J. Mech. Phys. Solids. **42**, 1397–1434 (1994). https://doi.org/10.1016/0022-5096(94)90003-5

28. Blanco, N., Turon, A., Costa, J.: An exact solution for the determination of the mode mixture in the mixed-mode bending delamination test. Composite Science and Technology **66**, 1256–1258 (2006). https://doi.org/10.1016/j.compscitech.2005.10.028

29. Camanho, P., Davila, C.G.: Mixed-Mode Decohesion Finite Elements in for the Simulation Composite of Delamination Materials. Nasa. TM-2002–21, 1–37 (2002). https://doi.org/10.1177/002199803034505

30. Irwin, G.R.: Plastic zone near a crack and freacture toughness. Proceedings of seventh Sagamore Ordnance material conference **4**, 63–78 (1960)

31. Hui, C.Y., Jagota, A., Bennison, S.J., Londono, J.D.: Crack blunting and the strength of soft elastic solids. Proc. R. Soc. A Math. Phys. Eng. Sci. **459**, 1489–1516 (2003). https://doi.org/10.1098/rspa.2002.1057

32. Falk, M.L., Needleman, A., Rice, J.R.: A critical evaluation of cohesive zone models of dynamic fracture. J. Phys. IV JP. **11**, 43–50 (2001). https://doi.org/10.1051/jp4:2001506

33. Hillerborg, A., Modéer, M., Petersson, P.-E.: Analysis of crack formation and crack growth in concrete by means of fracture mechanics and finite elements. Cem. Concr. Res. **6**, 773–781 (1976). https://doi.org/10.1016/0008-8846(76)90007-7

34. Cox, B.N., Marshall, D.B.: Concepts for bridged cracks in fracture and fatigue. Acta Metall. Mater. **42**, 341–363 (1994). https://doi.org/10.1016/0956-7151(94)90492-8

35. Z.P. Bažant, Planas J..: Fracture and size effect in concrete and other quasibrittle materials. Routledge (1998). https://doi.org/10.1201/9780203756799

36. Bazant, Z.P.: Size effect on structural strength: a review. Arch. Appl. Mech. **69**, 703–725 (1999). https://doi.org/10.1007/s004190050252

37. Yang, Q.D., Cox, B.N., Nalla, R.K., Ritchie, R.O.: Fracture length scales in human cortical bone : The necessity of nonlinear fracture models. Biomaterials **27**, 2095–2113 (2006). https://doi.org/10.1016/j.biomaterials.2005.09.040

38. Turon, A., Dávila, C.G., Camanho, P.P., Costa, J.: An engineering solution for mesh size effects in the simulation of delamination using cohesive zone models. Eng. Fract. Mech. **74**, 1665–1682 (2007). https://doi.org/10.1016/j.engfracmech.2006.08.025

39. Smith, E.: The size of the fully developed softening zone associated with a crack in a strain-softening material—II. A crack in a double-cantilever-beam specimen. Int. J. Eng. Sci. **27**, 309–314 (1989). https://doi.org/10.1016/0020-7225(89)90119-5

40. Planas, J., Elices, M.: Asymptotic analysis of a cohesive crack : 1. Theoretical background. International J. of Fracture **55**, 153–177 (1992). https://doi.org/10.1007/BF00017275

41. Planas, J., Elices, M.: Nonlinear fracture of cohesive materials. International J. of Fracture **51**, 139–157 (1991). https://doi.org/10.1007/BF00033975

42. Bao, G., Suo, Z.: Remarks on Crack-Bridging Concepts. Appl. Mech. Rev. **45**, 355–366 (1992). https://doi.org/10.1115/1.3119764

43. Suo, Z., Bao, G., Fan, B.: Delamination R-curve phenomena due to damage. J. Mech. Phys. Solids. **40**, 1–16 (1992). https://doi.org/10.1016/0022-5096(92)90198-B

44. Harper, P.W., Sun, L., Hallett, S.R.: A study on the influence of cohesive zone interface element strength parameters on mixed mode behaviour. Composites : Part A **43**, 722–734 (2012). https://doi.org/10.1016/j.compositesa.2011.12.016

45. Williams, J.G., Hadavinia, H.: Analytical solutions for cohesive zone models. J. Mech. Phys. Solids **50**, 809–825 (2002). https://doi.org/10.1016/S0022-5096(01)00095-3

46. Massabo, R.: Concepts for bridged Mode II delamination cracks. J. Mech. Phys. Solids. **47**, 1265–1300 (1999). https://doi.org/10.1016/S0022-5096(98)00107-0

47. Turon, A., Costa, J., Camanho, P.P., Maim, P.: Analytical and Numerical Investigation of the Length of the Cohesive Zone in Delaminated Composite Materials. Mechanical Response of Composites **10**, (2008). https://doi.org/10.1007/978-1-4020-8584-0_4

48. Harper, P.W., Hallett, S.R.: Cohesive zone length in numerical simulations of composite delamination. Eng. Fract. Mech. **75**, 4774–4792 (2008). https://doi.org/10.1016/j.engfracmech.2008.06.004
49. Abaqus: Abaqus 2017– Documentation, Dassault Systèmes Simulia Corporation
50. ASTM D6671M: Standard Test Method for Mixed Mode I-Mode II Interlaminar Fracture Toughness of Unidirectional Fiber Reinforced Polymer Matrix Composites
51. Turon, A., Camanho, P.P., Costa, J., Renart, J.: Accurate simulation of delamination growth under mixed-mode loading using cohesive elements : Definition of interlaminar strengths and elastic stiffness. **92**, 1857–1864 (2010). https://doi.org/10.1016/j.compstruct.2010.01.012
52. Lu, X., Ridha, M., Chen, B.Y., Tan, V.B.C., Tay, T.E.: On cohesive element parameters and delamination modelling. Eng. Fract. Mech. **206**, 278–296 (2019). https://doi.org/10.1016/j.engfracmech.2018.12.009
53. Thawre, M.M., Verma, K.K., Jagannathan, N., Peshwe, D.R., Paretkar, R.K., Manjunatha, C.M.: Effect of ply-drop on fatigue life of a carbon fiber composite under a fighter aircraft spectrum load sequence. Compos. Part B Eng. **86**, 120–125 (2016). https://doi.org/10.1016/j.compositesb.2015.10.002
54. Vidyashankar, B.R., Murty, A.V.K.: Analysis of laminates with ply drops. Composites Science and Technology **61**, 749–758 (2001). https://doi.org/10.1016/S0266-3538(01)00010-0
55. Ratcliffe, J.G., De Carvalho, N.V.: Investigating delamination migration in composite tape laminates. Technical Memorandum NASA-TM-2014–218289, (2014)
56. Wimmer, G., Kitzmüller, W., Pinter, G., Wettemann, T., Pettermann, H.E.: Computational and experimental investigation of delamination in L-shaped laminated composite components. **76**, 2810–2820 (2009). https://doi.org/10.1016/j.engfracmech.2009.06.007
57. Gözlüklü, B., Coker, D.: Modeling of the dynamic delamination of L-shaped unidirectional laminated composites. Compos. Struct. **94**, 1430–1442 (2012). https://doi.org/10.1016/j.compstruct.2011.11.015
58. Farmand-Ashtiani, E., Alanis, D., Cugnoni, J., Botsis, J.: Delamination in cross-ply laminates: Identification of traction-separation relations and cohesive zone modeling. Compos. Sci. Technol. **119**, 85–92 (2015). https://doi.org/10.1016/j.compscitech.2015.09.025
59. Geleta, T.N., Woo, K., Lee, B.: Delamination Behavior of L-Shaped Laminated Composites. Int. J. Aeronaut. Sp. Sci. **19**, 363–374 (2018). https://doi.org/10.1007/s42405-018-0038-y
60. Lindgaard, E., Bak, B.L.V.: Experimental characterization of delamination in off-axis GFRP laminates during mode I loading. Compos. Struct. **220**, 953–960 (2019). https://doi.org/10.1016/j.compstruct.2019.04.022
61. Pernice, M.F., De Carvalho, N.V., Ratcliffe, J.G., Hallett, S.R.: Experimental study on delamination migration in composite laminates. Compos. Part A Appl. Sci. Manuf. **73**, 20–34 (2015). https://doi.org/10.1016/j.compositesa.2015.02.018
62. Arki, S., Ferrero, J.F., Marguet, S., Redonnet, J.M., Aury, A.: Strengthening of a curved composite beam by introducing a flat portion. Compos. Struct. **222**, 110863 (2019). https://doi.org/10.1016/j.compstruct.2019.04.035
63. He, M.Y., Hutchinson, J.W.: Kinking of a Crack Out of an Interface. J. Appl. Mech. **56**, 270–278 (1989). https://doi.org/10.1115/1.3176078
64. Needleman, A.: Continuum Model for Void Nucleation By Inclusion Debonding. J. Appl. Mech. **54**, 525–531 (1987). https://doi.org/10.1115/1.3173064
65. Begley, M.R., Philips, N.R., Compton, B.G., Wilbrink, D.V., Ritchie, R.O., Utz, M.: Micromechanical models to guide the development of synthetic 'brick and mortar' composites. J. Mech. Phys. Solids. **60**, 1545–1560 (2012). https://doi.org/10.1016/j.jmps.2012.03.002
66. Tabiei, A.: Composite Laminate Delamination Simulation and Experiment : A Review of Recent Development. Appl. Mech. Rev. **70**, 1–23 (2018). https://doi.org/10.1115/1.4040448

Publisher's Note Springer Nature remains neutral with regard to jurisdictional claims in published maps and institutional affiliations.